



| | |
|------------------|--|
| Title | Wave activity in the tropical tropopause layer in seven reanalysis and four chemistry climate model data sets |
| Author(s) | Fujiwara, M.; Suzuki, J.; Gettelman, A.; Hegglin, M. I.; Akiyoshi, H.; Shibata, K. |
| Citation | Journal of Geophysical Research, Atmospheres, 117, D12105 https://doi.org/10.1029/2011JD016808 |
| Issue Date | 2012-06-26 |
| Doc URL | http://hdl.handle.net/2115/50989 |
| Rights | ©2012 American Geophysical Union |
| Type | article |
| File Information | JGRA117_D12105.pdf |



[Instructions for use](#)

Wave activity in the tropical tropopause layer in seven reanalysis and four chemistry climate model data sets

M. Fujiwara,¹ J. Suzuki,² A. Gettelman,³ M. I. Hegglin,^{4,5} H. Akiyoshi,⁶ and K. Shibata⁷

Received 31 August 2011; revised 10 May 2012; accepted 15 May 2012; published 26 June 2012.

[1] Sub-seasonal variability including equatorial waves significantly influence the dehydration and transport processes in the tropical tropopause layer (TTL). This study investigates the wave activity in the TTL in 7 reanalysis data sets (RAs; NCEP1, NCEP2, ERA40, ERA-Interim, JRA25, MERRA, and CFSR) and 4 chemistry climate models (CCMs; CCSRNIES, CMAM, MRI, and WACCM) using the zonal wave number-frequency spectral analysis method with equatorially symmetric-antisymmetric decomposition. Analyses are made for temperature and horizontal winds at 100 hPa in the RAs and CCMs and for outgoing longwave radiation (OLR), which is a proxy for convective activity that generates tropopause-level disturbances, in satellite data and the CCMs. Particular focus is placed on equatorial Kelvin waves, mixed Rossby-gravity (MRG) waves, and the Madden-Julian Oscillation (MJO). The wave activity is defined as the variance, i.e., the power spectral density integrated in a particular zonal wave number-frequency region. It is found that the TTL wave activities show significant difference among the RAs, ranging from ~ 0.7 (for NCEP1 and NCEP2) to ~ 1.4 (for ERA-Interim, MERRA, and CFSR) with respect to the averages from the RAs. The TTL activities in the CCMs lie generally within the range of those in the RAs, with a few exceptions. However, the spectral features in OLR for all the CCMs are very different from those in the observations, and the OLR wave activities are too low for CCSRNIES, CMAM, and MRI. It is concluded that the broad range of wave activity found in the different RAs decreases our confidence in their validity and in particular their value for validation of CCM performance in the TTL, thereby limiting our quantitative understanding of the dehydration and transport processes in the TTL.

Citation: Fujiwara, M., J. Suzuki, A. Gettelman, M. I. Hegglin, H. Akiyoshi, and K. Shibata (2012), Wave activity in the tropical tropopause layer in seven reanalysis and four chemistry climate model data sets, *J. Geophys. Res.*, *117*, D12105, doi:10.1029/2011JD016808.

1. Introduction

[2] Significant sub-seasonal variability is found in temperature, horizontal winds, and other parameters in the tropical tropopause layer (TTL) [Fueglistaler *et al.*, 2009]. This is

due to various types of equatorial waves, intraseasonal oscillations/the Madden-Julian Oscillation (MJO) [e.g., Madden and Julian, 1994], and other disturbances that are primarily generated by tropical organized convection [e.g., Kiladis *et al.*, 2009]. Previous case studies investigated various roles of equatorial Kelvin waves in the TTL, i.e., signals propagating eastward with 10–20-day periodicity, such as large temperature changes [Tsuda *et al.*, 1994], ozone transport [Fujiwara *et al.*, 1998], dehydration [Fujiwara *et al.*, 2001], turbulence generation [Fujiwara *et al.*, 2003; Flannaghan and Fueglistaler, 2011], and cirrus variations [Boehm and Verlinde, 2000; Immler *et al.*, 2008; Fujiwara *et al.*, 2009; Suzuki *et al.*, 2010a]. The Kelvin wave activity in the TTL has been investigated using Global Positioning System (GPS) radio occultation temperature data during 2001–2002 [Randel and Wu, 2005], during 2001–2005 [Ratnam *et al.*, 2006], and during 2006–2008/9 [Alexander *et al.*, 2008; Pan *et al.*, 2011], High Resolution Dynamics Limb Sounder (HIRDLS) data during 2005–2008 [Alexander and Ortland, 2010], and European Centre for Medium-Range Weather Forecasts (ECMWF) 40-year reanalysis (ERA40) data [Suzuki and Shiotani, 2008; Suzuki *et al.*, 2010b]. The climatology and

¹Faculty of Environmental Earth Science, Hokkaido University, Sapporo, Japan.

²Japan Agency for Marine-Earth Science and Technology, Yokosuka, Japan.

³National Center for Atmospheric Research, Boulder, Colorado, USA.

⁴Department of Physics, University of Toronto, Toronto, Ontario, Canada.

⁵Now at Department of Meteorology, University of Reading, Reading, UK.

⁶National Institute for Environmental Studies, Tsukuba, Japan.

⁷Meteorological Research Institute of Japan Meteorological Agency, Tsukuba, Japan.

Corresponding author: M. Fujiwara, Faculty of Environmental Earth Science, Hokkaido University, N10 W5, Sapporo 060-0810, Japan. (fuji@ees.hokudai.ac.jp)

excitation mechanisms of mixed Rossby-gravity (MRG) waves at 200 hPa were studied by *Magaña and Yanai* [1995] using ECMWF analysis data, and their seasonal and longitudinal variations above 15 km were studied by *Alexander et al.* [2008] using GPS temperature data. A case of MRG waves influencing the temperature and water vapor at the cold-point tropopause was discussed by *Selkirk et al.* [2010]. The MJO, i.e., signals propagating mostly eastward with 30–60-day periodicity, also affects the TTL region [e.g., *Kiladis et al.*, 2001, 2005]. For example, *Eguchi and Shiotani* [2004] studied the roles of the MJO in the TTL dehydration, *Virts and Wallace* [2010] and *Virts et al.* [2010] analyzed satellite TTL cirrus data at the MJO timescales, and *Suzuki and Shiotani* [2008] investigated the MJO activity in the TTL. The MJO in the TTL can be interpreted as the dynamical response to the tropical large-scale organized convection, often called the Matsuno-Gill pattern [*Matsuno*, 1966; *Gill*, 1980], which consists of a pair of anticyclonic cells located in both sides of the equator and eastward-westward winds along the equator. This pattern is the primary one that determines the transport pathway to the lower stratosphere over the tropical Pacific [*Hatsushika and Yamazaki*, 2003]. The same dynamical process also explains the seasonally averaged horizontal patterns of tropical tropopause temperature and horizontal winds [*Highwood and Hoskins*, 1998].

[3] Chemistry Climate Models (CCMs) have been extensively used to simulate the past ozone layer and to project the future ozone layer [e.g., *World Meteorological Organization*, 2007, 2011; *Eyring et al.*, 2010]. The performance of various CCMs in the tropical upper troposphere and lower stratosphere was recently evaluated by *Gottelman et al.* [2010]. The representation of the sub-seasonal variability in the TTL should be one of the key validation metrics for these CCMs. Reanalysis data sets (RAs) can be used for the validation of CCMs. There is, however, some evidence that different RAs (and operational analysis data sets) exhibit significantly different tropical tropopause temperature values on various timescales from day-to-day to annual mean [e.g., *Fujiwara et al.*, 2009, 2010]. Also, different RAs exhibit significantly different Brewer-Dobson circulation patterns particularly at low latitudes [*Iwasaki et al.*, 2009]. Therefore, the comparisons of different RAs are also of great interest.

[4] This paper investigates the sub-seasonal variability at the tropical 100 hPa level in 7 RAs and 4 CCMs (Table 1) for ~10 years during 1990–2000. The 7 RAs are (1) the National Centers for Environmental Prediction (NCEP) and National Center for Atmospheric Research (NCAR) reanalysis (NCEP1), (2) the NCEP and Department of Energy (DOE) Atmospheric Model Intercomparison Project (AMIP-II) reanalysis (NCEP2), (3) ERA40, (4) the most recent ECMWF “interim” reanalysis (ERA-Interim), (5) the Japanese 25-year reanalysis by Japan Meteorological Agency (JMA) and Central Research Institute of Electric Power Industry (CRIEPI) (JRA25), (6) the Modern Era Retrospective-analysis for Research and Applications by the National Aeronautics and Space Administration (NASA) (MERRA), and (7) the NCEP Climate Forecast System Reanalysis (CFSR). The 4 CCMs are (1) the Center for Climate System Research (CCSR), University of Tokyo and the National Institute for Environmental Studies (NIES) CCM (CCSRNIES), (2) the Canadian Middle Atmosphere Model (CMAM), (3) the Meteorological Research Institute of JMA CCM (MRI), and (4) the

Whole-Atmosphere Community Climate Model by NCAR (WACCM). These models were chosen because they provided four-times-daily instantaneous outputs or daily averaged outputs during the investigation period (Table 1). For the investigation of the tropical convective activity, the National Oceanic and Atmospheric Administration (NOAA) complete/interpolated outgoing longwave radiation (OLR) (NOAAOLR) data are also analyzed.

[5] The primary method of the investigation is the zonal wave number-frequency spectral analysis with equatorially symmetric-antisymmetric decomposition with a background spectrum estimation [e.g., *Wheeler and Kiladis*, 1999]. The remainder of this paper is organized as follows. Section 2 describes the data sets, and section 3 describes the details of the method. Section 4 provides results and discussion on the basic comparisons, the spectral analysis, and the wave activity calculations. Finally, section 5 lists the main conclusions.

2. Data Description

[6] Table 1 shows the information on the space-time resolution of the 7 RAs and 4 CCMs analyzed in this study. Some more key information is summarized below. At the end of this section, the NOAAOLR data set is also explained.

2.1. RAs

[7] The RAs are constructed as a best estimate of the past atmosphere using various operational ground-based, balloon, aircraft, and satellite observations with an assimilation scheme and a global forecast model. NCEP1 is based on the National Meteorological Center (NMC) operational Global Data Assimilation System and has been in operation since 1994 [*Kalnay et al.*, 1996; *Kistler et al.*, 2001]. NCEP2 has been in operation since 1998 as an upgraded version of NCEP1 by correcting human processing errors in NCEP1 [*Kanamitsu et al.*, 2002]. ERA40 is based on the ECMWF data assimilation and forecasting system used in 2001–2002 and was completed in 2003, covering the period from September 1957 to August 2002 [*Uppala et al.*, 2005]. ERA-Interim is an upgraded version of ERA40 with several advances including using a 12-hour four-dimensional (4D) variational analysis scheme (4D-Var), while ERA40 used a 6-hour three-dimensional (3D) variational analysis scheme (3D-Var), and has been in operation since 2006, covering the period from 1989 to present [*Dee et al.*, 2011] (in August 2011, ERA-Interim has been extended to 1979). JRA25 is based on the JMA operational data assimilation system used in 2002, originally covered the period from 1979 to 2004, and was transitioned to the JMA Climate Data Assimilation System (JCDAS) for the period after 2004 [*Onogi et al.*, 2007]. MERRA is based on the Goddard Earth Observing System data assimilation system version 5 (GEOS-5) and has been in operation since 2008, covering the period from 1979 to present [*Rienecker et al.*, 2011]. CFSR is a new coupled atmosphere-ocean reanalysis of NCEP for the period of 1979–present, with a much higher horizontal and vertical resolution of the atmosphere than that of NCEP1 and NCEP2 [*Saha et al.*, 2010]. Note that the analysis scheme used in CFSR for the atmosphere, the grid point (gridded) statistical interpolation scheme (categorized as a 3D-Var with a 6-hour update cycle), is nearly the same as the one used in MERRA and that

Table 1. Information on the RAs and CCMs

| Data Set | Model Resolution ^a | Model Top | Model dz in the TTL ^b | Output Grid ^c |
|---------------------------------|-------------------------------|----------------------------|----------------------------------|---------------------------|
| <i>Reanalysis</i> | | | | |
| NCEP1 | T62, L28 | 3 hPa | ~1.8 km | 2.5° × 2.5°, L17, 6 hr |
| NCEP2 | T62, L28 | 3 hPa | ~1.8 km | 2.5° × 2.5°, L17, 6 hr |
| ERA40 | T ₁ 159, L60 | 0.1 hPa | ~1.1 km | 2.5° × 2.5°, L23, 6 hr |
| ERA-Interim | T ₁ 255, L60 | 0.1 hPa | ~1.1 km | 1.5° × 1.5°, L37, 6 hr |
| JRA25 | T106, L40 | 0.4 hPa | ~1.3 km | 1.25° × 1.25°, L23, 6 hr |
| MERRA | (2/3)° × 0.5°, L72 | 0.01 hPa | ~1.1 km | (2/3)° × 0.5°, L42, 6 hr |
| CFSR | T382, L64 | ~0.266 hPa | ~0.88 km | 0.5° × 0.5°, L37, 6 hr |
| <i>Chemistry Climate Models</i> | | | | |
| CCSRNIES | T42, L34 | ~0.012 hPa | ~1.2 km | ~2.8° × ~2.8°, L31, 1 dy |
| CMAM | T31, L71 | 8.1 × 10 ⁻⁴ hPa | ~1.2 km | ~5.6° × ~5.6°, L63, 6 hr |
| MRI | T42, L68 | 0.01 hPa | ~0.79 km | ~2.8° × ~2.8°, L24, 1 dy |
| WACCM | 144 × 96 grids, L66 | 4.5 × 10 ⁻⁶ hPa | ~1.1 km | 2.5° × ~1.895°, L66, 6 hr |

^aT means the truncation horizontal wave number, and T_n corresponds to $\sim(120/n)^\circ$ grids (except for CMAM whose resolution is $\sim 5.6^\circ \times \sim 5.6^\circ$). The horizontal resolution for ERA40 (ERA-Interim) is T₁159(255) with N80(128) reduced Gaussian grids, which corresponds to ~ 125 (~ 79) km globally. L means the number of vertical levels.

^bAverage resolution between ~ 200 hPa and ~ 50 – 60 hPa.

^cThe horizontal grids in longitude × latitude, number of vertical levels, and temporal resolution for the data sets analyzed in this study. The 6-hr data sets have four-times-daily instantaneous outputs, while the 1-dy data sets have daily averaged outputs.

ERA40 stratospheric wind profiles were used as bogus observations for the period of 1981–1998 to obtain a reasonable signature of the Quasi-Biennial Oscillation (QBO) [Saha *et al.*, 2010].

[8] Among the above RAs, NCEP1, NCEP2, ERA40, JRA25 use 3D-Var, and ERA-Interim uses 4D-Var. For MERRA and CFSR, the grid point statistical interpolation analysis scheme (a 3D-Var) is used [Saha *et al.*, 2010; Rienecker *et al.*, 2011].

[9] The large-scale wave activity in the TTL may depend largely on the vertical resolution in the TTL of the global forecast model used in each RA. The information on the model vertical resolution in the TTL, shown in Table 1, is obtained from Kalnay *et al.* [1996] for NCEP1 and NCEP2, A. Simmons (private communication, 2011), for ERA40 and ERA-Interim, K. Onogi (private communication, 2011) for JRA25, M. G. Bosilovich (private communication, 2011) for MERRA, and S. Moorthi (private communication, 2011) for CFSR. The vertical levels in the provided data in the TTL are 200, 150, 100, and 70 hPa for all RAs except for ERA-Interim and CFSR where additional levels at 175 and 125 hPa are present.

[10] The zonal mean temperature climatology for four seasons show that the coldest point in the tropics is located at 100 hPa for all the 7 RAs, though the next upper level available is 70 hPa for all the 7 RAs. Therefore, the 100 hPa level is chosen as the tropical tropopause in this paper.

2.2. CCMs

[11] The calculations and outputs were specially made for this study for all the 4 CCMs. The calculations were made under the so-called REF-B1 scenario [Eyring *et al.*, 2010; Morgenstern *et al.*, 2010] which uses the observed changes in sea surface temperatures, ozone depleting substances, and greenhouse gases as the boundary/prescribed conditions. The period considered in the following analyses is between January 1, 1990 and February 28, 2000. The output parameters include 4D temperature, zonal wind, and meridional wind, and 3D OLR. Brief explanations about each CCM are written below.

[12] CCSRNIES uses a prognostic Arakawa-Schubert scheme for the cumulus parameterization (see Akiyoshi *et al.* [2009] for details). For this paper, the calculations were made at the horizontal resolution of T42 ($\sim 2.8^\circ \times \sim 2.8^\circ$) with 34 sigma levels from 0.995 to 1.24485×10^{-5} ; the output levels for the 4D parameters are 31 pressure levels from 1000 hPa to 0.1 hPa. There are 8 model levels between ~ 200 hPa and ~ 60 hPa, corresponding to the average vertical resolution of ~ 1.2 km. The QBO is simulated through nudging to observations [see Akiyoshi *et al.*, 2009].

[13] CMAM uses the Zhang-McFarlane scheme for the cumulus parameterization. For this paper, the calculations were made with CMAM version 8 at 32×64 linear Gaussian transform grid ($\sim 5.6^\circ \times \sim 5.6^\circ$) with 71 mixed sigma-pressure levels from the surface to 8.1×10^{-4} hPa; The output levels for 4D parameters are 63 pressure levels from 1000 hPa to 8.1×10^{-4} hPa. The average vertical resolution between 10 km and 20 km is ~ 1.2 km [Scinocca *et al.*, 2008, Figure 1]. There is no special treatment for simulating the QBO. The zonal mean zonal wind plot (not shown) exhibits only westward winds in the lower stratosphere near the equator (~ 0 m s⁻¹ near the tropopause to ~ -10 m s⁻¹ at 30–20 hPa) with very weak annual and QBO-time-scale variations. The prevailing westward winds above the tropopause in this model might somewhat affect the statistical wave activity in the TTL; this is because Kelvin wave amplitudes are known to have a QBO-phase dependence, with greater amplitudes in the eastward shear phase [e.g., Ratnam *et al.*, 2006].

[14] MRI uses a prognostic Arakawa-Schubert scheme for the cumulus parameterization (see Shibata *et al.* [2005] for details). For this paper, the calculations were made at the horizontal resolution of T42 ($\sim 2.8^\circ \times \sim 2.8^\circ$) with 68 hybrid sigma-pressure levels from the surface to 0.01 hPa; the output levels for the 4D parameters are 24 pressure levels from 1000 hPa to 0.01 hPa. There are 15 model levels between ~ 200 hPa and ~ 50 hPa, corresponding to the average vertical resolution of ~ 0.79 km. (Note that the vertical resolution is set as 0.50 km between 100 hPa and 10 hPa.) A QBO-like variation is internally generated by

both parameterized and resolved atmospheric waves. The zonal mean zonal wind plot (not shown) exhibits somewhat slower descending signals, with only about 4 cycles of the QBO during the period of 1990–2000 (about 5 cycles in the reality). Furthermore, the eastward wind phases of the QBO-like variation only reach the 60–70 hPa level and do not reach the 100 hPa level as in the real atmosphere; this might somewhat affect the statistical wave activity in the TTL. It should be noted that for the radiation calculations including OLR, the effective horizontal resolution is a fourth of T42 (i.e., $\sim 11.2^\circ$); this should not influence the following analyses significantly because we only focus on zonal wave numbers less than 15 (i.e., $>24^\circ$).

[15] WACCM uses the Zhang-MacFarlane scheme for the cumulus parameterization (see *Garcia et al.* [2007] for details). For this paper, the calculations were made at the horizontal grids of 144×96 ($2.5^\circ \times \sim 1.895^\circ$) with 66 hybrid sigma-pressure levels from the surface to $\sim 5.96 \times 10^{-6}$ hPa; the 4D output data are linearly interpolated on to 66 pressure levels from 990 hPa to $\sim 5.96 \times 10^{-6}$ hPa before the analyses. There are 10 model levels between ~ 200 hPa and ~ 50 hPa, corresponding to the average vertical resolution of ~ 1.1 km. The QBO is simulated through nudging to observations.

[16] The zonal mean temperature climatology for four seasons show that the coldest point in the tropics is located at 100 hPa for CMAM and MRI (though the next upper level available for MRI is 70 hPa) but at somewhat higher levels for CCSRNIIES (80 hPa) and WACCM (86 hPa). In Section 4.1 for the basic comparisons including the climatology, we will briefly discuss the results from these upper levels in the CCSRNIIES and WACCM data sets. We have also investigated the spectra and wave activities at 80 hPa for CCSRNIIES and CMAM, 70 hPa for MRI, and 86 hPa for WACCM, and found that there are common tendencies with respect to the 100 hPa results for all the 4 data sets (e.g., a tendency that MRG wave signals stand out clearly in temperature and meridional wind, and a tendency that the wave activities in temperature become much larger). This implies that the 80 hPa level for CCSRNIIES and the 86 hPa level for WACCM show more lower stratospheric characteristics rather than the tropopause characteristics. Therefore, the 100 hPa level is chosen as the tropical tropopause also for the 4 CCMs in this paper.

2.3. NOAAOLR

[17] The OLR is used as a proxy for large-scale tropical convective activity that is the source of large-scale tropical waves in the TTL (and the above and below). Although the variability of convective precipitation is more directly linked to the wave activity in the middle atmosphere [*Horinouchi et al.*, 2003], we chose the OLR as a diagnostic parameter for direct comparisons with the observations. The NOAAOLR is a complete/interpolated OLR data set based on NOAA polar-orbiting satellite measurements by making both spatial and temporal interpolations [*Liebmann and Smith*, 1996]. The data are available daily at the horizontal resolution of $2.5^\circ \times 2.5^\circ$. As discussed by *Wheeler and Kiladis* [1999, section 2], some erroneous peaks are found in the NOAAOLR power spectral results due to the satellite measurements in 14 swaths per day around the globe, the slow orbital precession with ~ 9 -day period, and the folding of various harmonics

about the frequency of 0.5 cycle per day (day^{-1}). Following their study, the power values at positive zonal wave numbers 13–15 and periods of 7–10 and 4–5 day for both symmetric and antisymmetric components were flagged as special values (after the background red-noise spectrum estimation and before the wave activity calculations) and not plotted. (Note that we will only show the power spectra for the range $0\text{--}0.5 \text{ day}^{-1}$ and that we will only use the power within ± 10 zonal wave numbers for the wave activity calculations.)

3. Method

3.1. Zonal Wave Number-Frequency Spectrum

[18] The zonal wave number-frequency spectrum is obtained by basically following the method presented by *Wheeler and Kiladis* [1999]. Data, $A(x, y, t)$ at, e.g., 100 hPa, within $\sim 15^\circ\text{N}\text{--}\sim 15^\circ\text{S}$ are decomposed into an equatorially symmetric component, $A_s(x, y, t)$, and an antisymmetric component, $A_a(x, y, t)$, where A is either temperature, zonal wind, meridional wind, or OLR, x is longitude, y is latitude, and t is time, as: $A_s(x, y, t) = [A(x, y, t) + A(x, -y, t)]/2$ and $A_a(x, y, t) = [A(x, y, t) - A(x, -y, t)]/2$. Several sets of these two components are obtained for latitudinal pairs at $y = \sim 0^\circ$ to $\sim 15^\circ$ and for temporal segments. In the following, the results from the spectral calculations for 120 sets of two-month overlapping 92-day segments between January 1990 and February 2000 will be discussed.

[19] Each temporal segment of A_s or A_a is detrended and tapered with the Welch-type data window [*Press et al.*, 1992]. (We have confirmed that different data windows described by *Press et al.* [1992] give virtually the same final spectral results.) Complex fast Fourier transforms (FFTs) [*Press et al.*, 1992] are then performed in longitude and then in time. Note that in this study, the positive (negative) zonal wave number regions correspond to eastward-moving (westward-moving) signals; the frequency is positive only. The obtained spectrum for each latitudinal pair for each temporal segment is adjusted with a constant factor so that the integration for zonal wave number (in cycle per 360° -longitude, i.e., 1) and for frequency (in cycle per day, i.e., day^{-1}) in the whole domain equals to the variance of the original time series (the variance is calculated after detrending and before windowing). Therefore, the final spectrum is the power spectral density (e.g., in $\text{K}^2 \text{ day}$ for the case of temperature) and can be compared for the same parameter from different data sets. The adjusted spectrum is then averaged for all the latitudinal pairs and temporal segments for symmetric and antisymmetric components separately, and is smoothed by one pass of a 1-2-1 running mean filter both in zonal wave number and in frequency to improve the presentation. This smoothing is applied for the base 10 logarithm of the spectrum as suggested by *Chao et al.* [2008]. The smoothed base 10 logarithm of the spectrum is what is shown with contours in the following spectrum figures.

3.2. Background Spectrum

[20] The obtained spectrum has a component of background “red noise” with larger values at lower frequencies at each zonal wave number (and, similarly, at lower zonal wave numbers at each frequency). This is due to the fact that the meteorological parameters at a certain time are more or

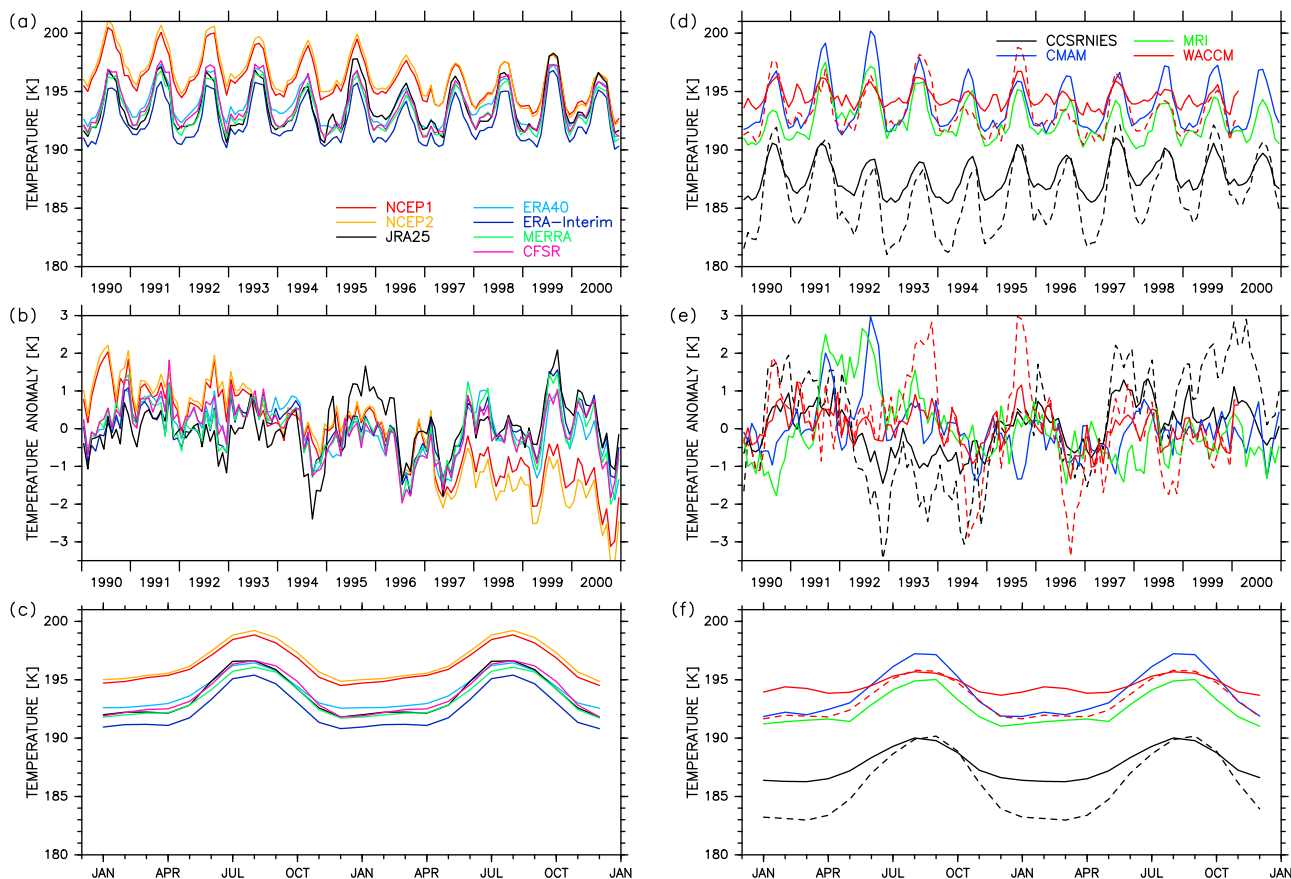


Figure 1. Time series of (a, d) monthly and zonal mean temperature at 100 hPa within 10°N – 10°S (10.5°N – 10.5°S for ERA-Interim), (b, e) temperature anomaly with respect to the 1990–1999 climatology, and (c, f) the 1990–1999 climatology (repeated twice), from 7 RAs (Figures 1a–1c) and from 4 CCMs (Figures 1d–1f). In the CCM panels (Figures 1d–1f), the results from CCSRNIES at 80 hPa (black dotted) and WACCM at 86 hPa (red dotted) are also shown.

less influenced by their own immediate past value; this process is called a first-order auto-regressive (or first-order linear Markov) process [e.g., Gilman *et al.*, 1963; von Storch and Zwiers, 1999]. The signals related to meteorological disturbances are found as bulges on the background slope associated with the red-noise spectrum or, in other words, as ridges or hills in the zonal wave number-frequency spectrum.

[21] Several methods have been used to estimate the background spectrum for the zonal wave number-frequency spectrum [e.g., Wheeler and Kiladis, 1999; Hendon and Wheeler, 2008; Chao *et al.*, 2008]. In this paper, we choose the method with many passes of the 1-2-1 filter that was used by Wheeler and Kiladis [1999]. Furthermore, as proposed by Chao *et al.* [2008], the background spectrum is estimated for symmetric and antisymmetric components separately; we do not combine the two smoothed spectra to obtain a common background spectrum as was done by Wheeler and Kiladis [1999].

[22] Wheeler and Kiladis [1999] wrote, ‘the number of passes of the 1-2-1 filter we have used is 10 in frequency throughout, and from 10 to 40 in wave number, being 10 at low frequencies and 40 at higher frequencies increasing in two different steps’ for their *twice-daily* $2.5^{\circ} \times 2.5^{\circ}$ NOAA OLR data set with 96-day segments between 15°N and 15°S . We have set the number of passes as 10 in frequency and

40 in zonal wave number throughout for our daily $2.5^{\circ} \times 2.5^{\circ}$ NOAA OLR data set with 92-day segments between 15°N and 15°S . We then set the number of passes for each data set so as to be inversely proportional to the number of passes for the NOAA OLR data set according to the wave number/frequency resolution. See Appendix A for the actual number of passes that we have used for each data set in this study.

[23] We note that there are uncertainties in the method for calculating the background spectrum. Our method differs from that used by Wheeler and Kiladis [1999], and the significance at the low frequency end in the following spectrum figures (e.g., Figure 6) may be a consequence of the technique (which is similar to Chao *et al.* [2008]). There is currently large uncertainty in the proper way to estimate this part of the background spectrum. However, the key aspect of this work is analysis of models and reanalyses using the same methodology.

3.3. Statistical Significance and Dispersion Relation of Equatorial Waves

[24] In the following spectrum figures, we show the base 10 logarithm of the power spectral density in contours, and the statistically significant ‘bulge’ regions defined as those having a ratio of ≥ 1.1 (for non-logarithm values) with respect to the background power spectral density in gray

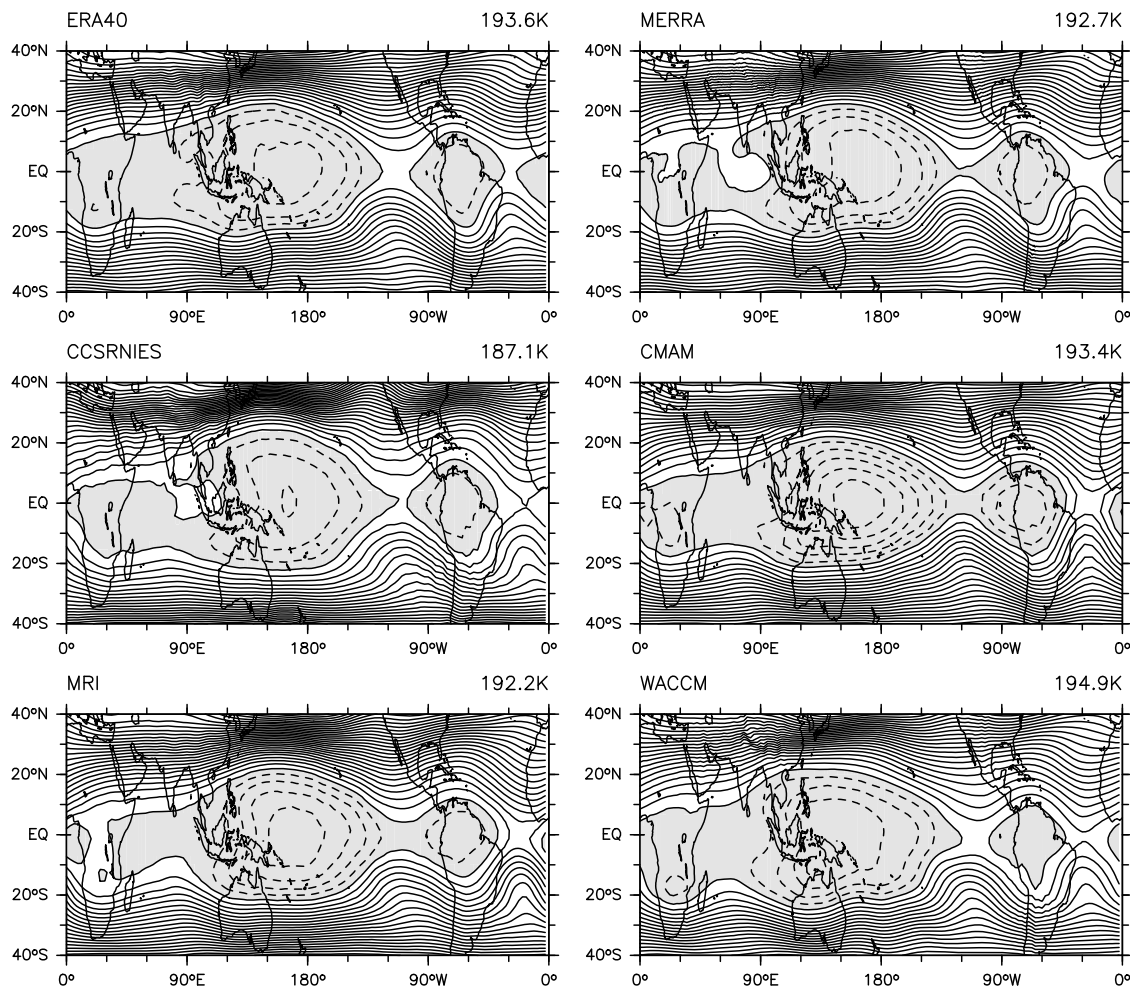


Figure 2. Distribution of temperature at 100 hPa averaged for December-January-February (DJF) during the period between January 1990 and February 2000 from 2 RAs (ERA40 and MERRA) and 4 CCMs. Anomaly from the 20°N–20°S average for each data set (shown on the top right of each panel) is shown. The contour interval is 1 K. The regions with negative anomalies are colored gray.

tones. This enables us to see the original spectrum and the signals evaluated as significant at the same time. The ratio number 1.1 is chosen by following *Wheeler and Kiladis* [1999].

[25] Also shown in the spectrum figures are the dispersion relation curves for various theoretical equatorial waves on the basis of a shallow water model on the equatorial β plane under the zero background-wind condition [*Matsuno*, 1966]. The symmetric modes for temperature, zonal wind, and OLR include eastward-moving equatorial Kelvin waves, westward-moving equatorial Rossby waves at lower frequencies, and eastward- and westward-moving inertio-gravity waves with the meridional mode number $n = 1$ at higher frequencies. The antisymmetric modes for the above three parameters and the symmetric modes for meridional wind include westward-moving MRG waves and eastward-moving inertio-gravity waves with $n = 0$. For meridional wind, the symmetric-antisymmetric decomposition is switched from that for temperature, zonal wind, and OLR due to the definition of the meridional wind direction; also, Kelvin waves do not have the meridional wind component in the linear wave theory. For each wave type, we draw three curves corresponding to the three equivalent depths, $h = 8$,

70, and 240 m by following *Suzuki and Shiotani* [2008] (in some cases, curves with larger h are located outside the figure domain shown). h in a shallow water model corresponds to the vertical wave number m in a stratified fluid through the background buoyancy frequency N , magnitude of gravity g , and scale height H as $gh \leftrightarrow N^2/[m^2 + 1/(4H^2)]$. $h = 8$, 70, and 240 m correspond to the vertical wavelengths of 2.5 (5.6), 7.4 (17), and 14 (32) km, respectively, at $N^2 = 5.0 \times 10^{-4}$ (1.0×10^{-4}) s^{-2} .

4. Results and Discussion

4.1. Basic Comparisons

[26] Figure 1 shows the time series of monthly and zonal mean temperature at 100 hPa within 10°N–10°S (10.5°N–10.5°S for ERA-Interim) together with the deseasonalized time series and the climatology for the 7 RAs and 4 CCMs. NCEP1 and NCEP2 show significantly higher tropopause temperature values (~ 3 K on average; almost independent of season) with unrealistically large negative trends in the 1990s as also discussed by *Fujiwara et al.* [2010]. JRA25 shows greater negative anomalies in 1994 and greater positive

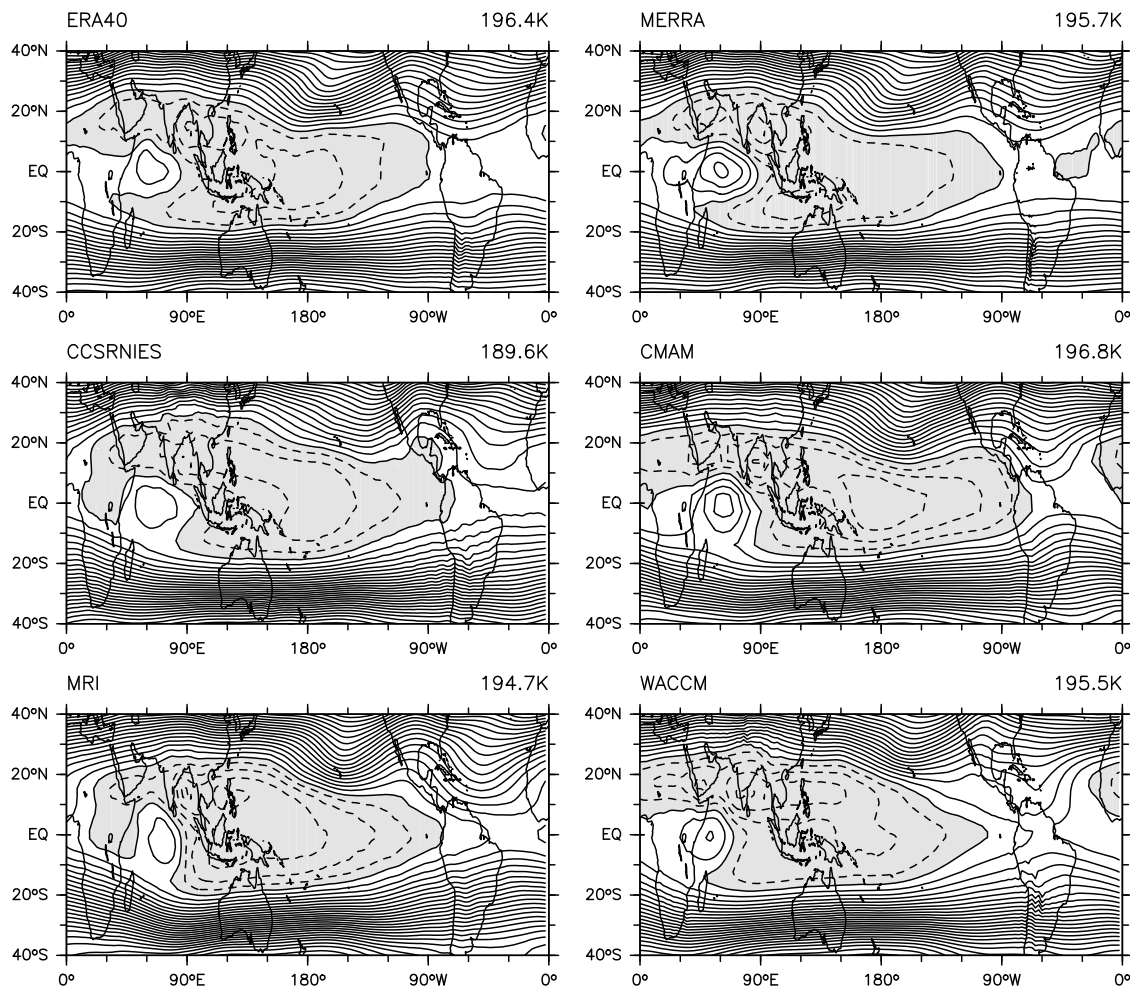


Figure 3. As for Figure 2, but for June-July-August (JJA).

anomalies in 1995 through early 1996 compared to the other RAs; this is probably related to the satellite radiance data assimilation [see *Onogi et al.*, 2007, section 4.8]. Except for these periods, the deseasonalized time series from the 5 RAs (excluding NCEP1 and NCEP2) show qualitatively similar interannual variations with greater variability in the latter half of the 1990s and with a drop around 2000 [e.g., *Fujiwara et al.*, 2010]. The climatology panel shows that ERA-Interim is 1–2 K colder than ERA40 and that the seasonal amplitude of ~ 2 K is common for all the 7 RAs. The panels for the 4 CCMs also include the results from CCSRNIES at 80 hPa and WACCM at 86 hPa, in addition to the model results at 100 hPa. The results from the CCMs at 100 hPa show much greater variety than those for the RAs. At 100 hPa, CCSRNIES is ~ 6 K colder, and WACCM shows a much smaller seasonal amplitude of ~ 1 K than the other CCMs. CCSRNIES at 80 hPa and WACCM at 86 hPa shows even lower values during the northern winter to spring; this results in a much better seasonal-cycle representation for WACCM. Furthermore, the deseasonalized time series panels show that the CCMs do not reproduce the interannual variations in the observations well; this might suggest that the interannual variations during the period of 1999–2000 were mostly the internal variability of the atmosphere and not due to a particular forcing. It should be noted that a 1 K difference

at tropical 100 hPa corresponds to ~ 1 ppmv saturation water vapor mixing ratio difference. Thus, even the difference between ERA40 and ERA-Interim can be serious for the stratospheric water vapor budget issues.

[27] Figures 2 and 3 show the December-January-February (DJF)-mean and June-July-August (JJA)-mean distributions, respectively, of temperature at 100 hPa in the tropics from 2 RAs (ERA40 and MERRA) and 4 CCMs during the period between January 1990 and February 2000. ERA40 and MERRA are chosen as examples of older RA and newer RA, respectively (these two showed quite similar features in Figure 1). To remove the bias component shown in Figure 1, the 20°N – 20°S average is subtracted for each data set. Furthermore, Figure 4 shows the same temperature-anomaly distributions as in Figures 2 and 3, but at/near the equator from all the 11 data sets at 100 hPa, CCSRNIES at 80 hPa, and WACCM at 86 hPa; and Table 2 shows the 20°N – 20°S average values. The climatological patterns in the temperature anomalies are a result of the combined forcings from different wave sources in the tropics [*Highwood and Hoskins*, 1988], and therefore can be used as a first indicator of how different the representation of these waves are in the 11 data sets. In DJF (Figure 2), there are common features of the primary cold region over the western Pacific through the Indonesian maritime continent and the secondary

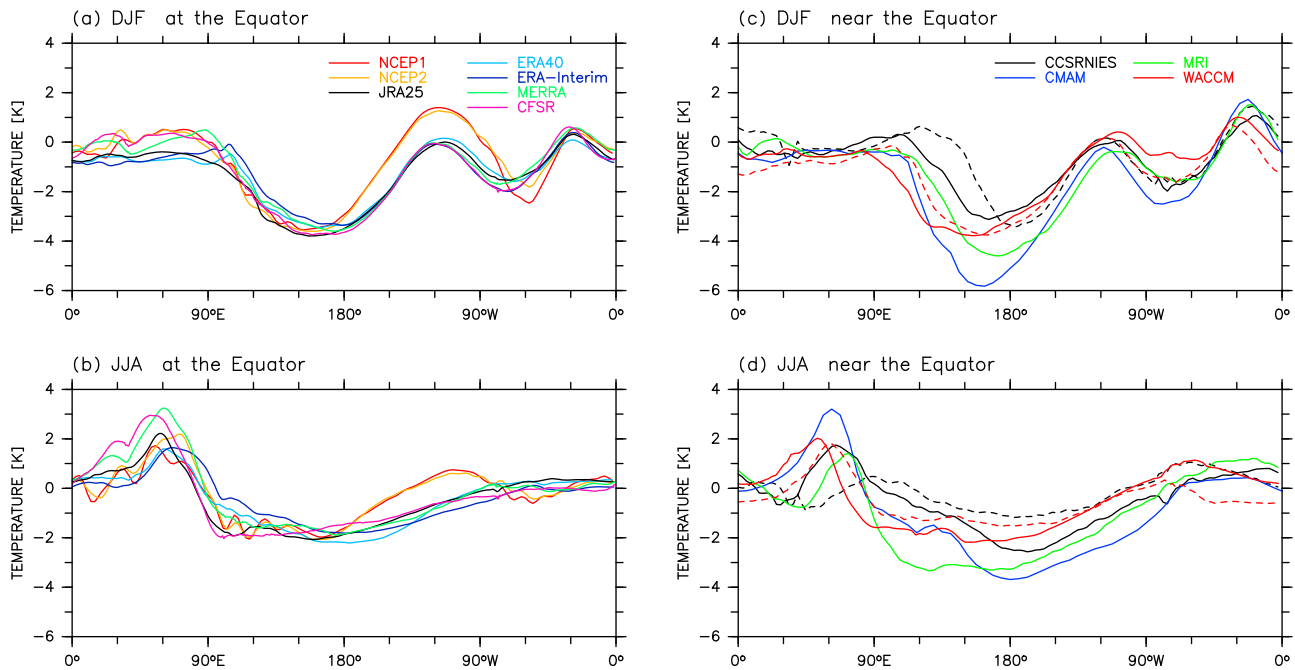


Figure 4. Distribution of temperature at 100 hPa at/near the equator averaged (a, c) for December–January–February (DJF) and (b, d) for June–July–August (JJA) during the period between January 1990 and February 2000 from 7 RAs (Figures 4a and 4b) and 4 CCMs (Figures 4c and 4d). Anomaly from the 20°N–20°S average for each data set (see Table 2) is shown. Dotted curves in Figures 4c and 4d are for CCSRNIES at 80 hPa (black) and for WACCM at 86 hPa (red). The exact latitude values are 0° (i.e., the equator) for all the RAs, 1.3953°N for CCSRNIES and MRI, 2.7689°N for CMAM, and 0.9474°N for WACCM.

cold region centered over the northern South America [e.g., *Nishimoto and Shiotani*, 2012]. For all the RAs, the secondary cold region is ~ 2 K warmer than the primary cold region. The contrast between the primary cold region and the eastern Pacific warm region is somewhat different among the RAs, being largest for NCEP1 and NCEP2. Also, the primary cold region is located slightly to the west and the secondary cold region is located $\sim 15^\circ$ to the east in NCEP1 and NCEP2 compared with the other RAs (Figure 4). For CCMs, the secondary cold region is 3–4 K warmer than the primary cold region except for CCSRNIES which shows a similar contrast to the RAs. The results from the higher levels in the CCSRNIES and WACCM both show an eastward shift of the primary cold region. In JJA (Figure 3), there are common features of an equatorially asymmetric cold region extending from the Arabian Peninsula through India to the equatorial eastern Pacific and a warm region over the equatorial western Indian Ocean [e.g., *Nishi et al.*, 2010; *Nishimoto and Shiotani*, 2012] with a generally weaker cold region over the subtropical southern hemisphere Indian Ocean in both RAs and CCMs. The contrast between the coldest region centered at the Bay of Bengal and the warmest region over the equatorial western Indian Ocean is quite different even among the RAs, ranging from 4–5 K in ERA40 and ERA-Interim (not shown) to 7–8 K in MERRA. Also, the temperature distributions over the southern hemisphere tropical Indian Ocean to the northern Australia and over the tropical western Pacific are different among the RAs (Figure 3, shown for a sub-selection of RAs only). For the CCMs, the tropical western-to-central Pacific

tends to be colder for CMAM and MRI. Also, the tropical northwestern Africa tends to be warmer for CCSRNIES and MRI. The equatorial distribution (Figure 4) shows that the contrast between the maximum over the equatorial Indian Ocean and the equatorial western Pacific is different for different data sets, and NCEP1 and NCEP2 shows a broad maximum also over the equatorial eastern Pacific. The results from the higher levels in the CCSRNIES and WACCM both show an eastward shift of the equatorial Indian Ocean maximum.

[28] Figure 5 shows a case of large-amplitude equatorial Kelvin waves at/near Bandung (6.9°S, 107.6°E), Indonesia

Table 2. Average Temperature Values (in Kelvin) for 20°N–20°S at 100 hPa (or Other Levels If Specified) in DJF and JJA During January 1990 to February 2000

| Data Set | DJF | JJA |
|-------------------|-------|-------|
| NCEP1 | 195.3 | 198.5 |
| NCEP2 | 195.6 | 198.8 |
| ERA40 | 193.6 | 196.4 |
| ERA-Interim | 192.0 | 195.1 |
| JRA25 | 193.2 | 196.5 |
| MERRA | 192.7 | 195.7 |
| CFSR | 192.9 | 196.2 |
| CCSRNIES | 187.1 | 189.6 |
| CCSRNIES (80 hPa) | 184.1 | 188.7 |
| CMAM | 193.4 | 196.8 |
| MRI | 192.2 | 194.7 |
| WACCM | 194.9 | 195.5 |
| WACCM (86 hPa) | 192.9 | 195.4 |

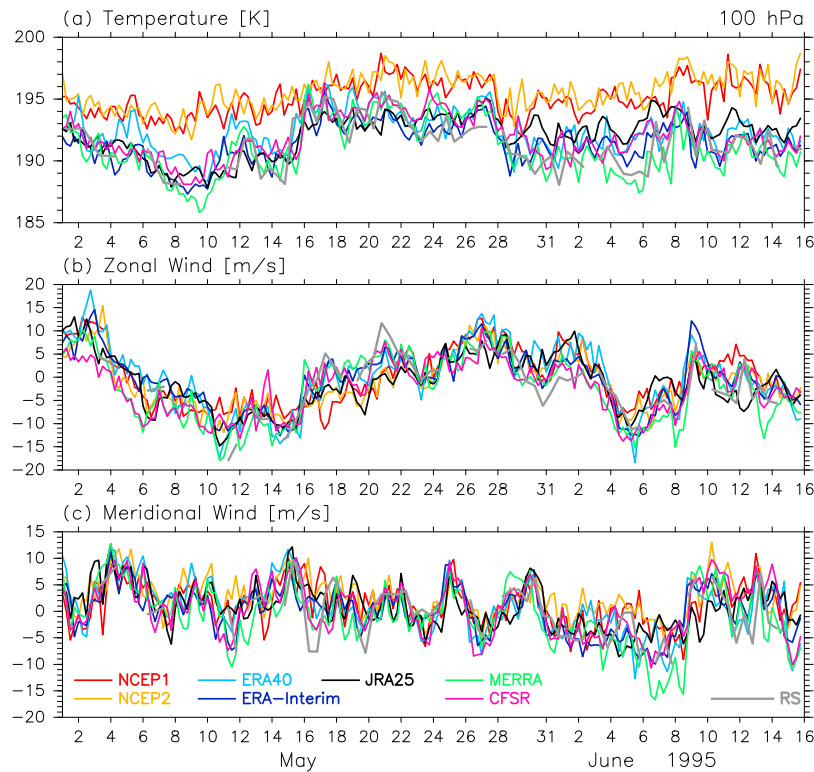


Figure 5. Time series of (a) temperature, (b) zonal wind, and (c) meridional wind at 100 hPa at/near Bandung (6.9°S, 107.6°E), Indonesia between 1 May and 15 June 1995 from radiosondes (gray) and 7 RAs. The horizontal grid point is (7.5°S, 107.5°E) for NCEP1, NCEP2, ERA40, and JRA25, (7.5°S, 108°E) for ERA-Interim, (7°S, 107.33°E) for MERRA, and (7°S, 107.5°E) for CFSR.

in May–June 1995 when *Fujiwara et al.* [1998] discovered an irreversible ozone transport process from the tropical lower stratosphere to the tropical upper troposphere in association with breaking Kelvin waves. Radiosonde temperature, zonal wind, and meridional wind data at 100 hPa as well as those data at nearest horizontal grid point from the 7 RAs are shown. Note that these radiosonde data were not transmitted over the Global Telecommunications System of the World Meteorological Organization and therefore provide an observational data source ideal for independent validation. The temperature oscillation (with minima around 8–10 May and 30 May–6 June and a maximum around 16–22 May) and the zonal wind oscillation (with westward wind maxima around 10–16 May and 4–8 June and an eastward wind maximum around 26–28 May) are due to equatorial Kelvin waves. In the meridional wind, shorter-period disturbances can be observed. For this particular case, the Kelvin wave temperature amplitude is smaller for NCEP1 and NCEP2 (apart from their warm bias) and somewhat larger for MERRA; for zonal and meridional winds, the difference among the RAs is not obvious, but MERRA

shows larger amplitudes for shorter-period disturbances (e.g., in June for the meridional wind).

4.2. Spectral Analysis

[29] Figures 6–13 show the zonal wave number–frequency spectrum for various parameters within 15°N–15°S for all seasons between January 1990 and February 2000, with 120 sets of two-month overlapping 92-day segments, for either the symmetric or antisymmetric component from the 7 RA and 4 CCM data sets. Note again that eastward-moving (westward-moving) disturbances appear in the positive (negative) zonal wave number region. In the following, the results are described and discussed for each parameter separately.

4.2.1. Temperature at 100 hPa

[30] Figures 6 and 7 show the spectrum for temperature at 100 hPa for the symmetric and antisymmetric component, respectively, from the 7 RAs, while Figures 8 and 9 show the same from the 4 CCMs. As explained in section 3, the zonal wave number–frequency spectrum shows larger values at lower frequencies and at lower zonal wave numbers. The signals of various disturbances are found as bulges or ridges

Figure 6. Zonal wave number–frequency spectrum of temperature at 100 hPa within 15°N–15°S during the period between January 1990 and February 2000 for the symmetric component for 7 RAs. Contours show the base 10 logarithm of the power spectral density (interval is 0.2). The regions where the ratio to the estimated background spectrum is ≥ 1.1 are colored gray (interval 0.1 with darkest gray indicating values ≥ 1.4). Dotted curves show the equatorial-wave dispersion relation at equivalent depth, $h = 8, 70,$ and 240 m for Kelvin waves (positive wave numbers) and equatorial Rossby waves (negative wave numbers). Dispersion relation for meridional-mode-number $n = 1$ inertio-gravity waves at $h = 8$ spans all wave numbers.

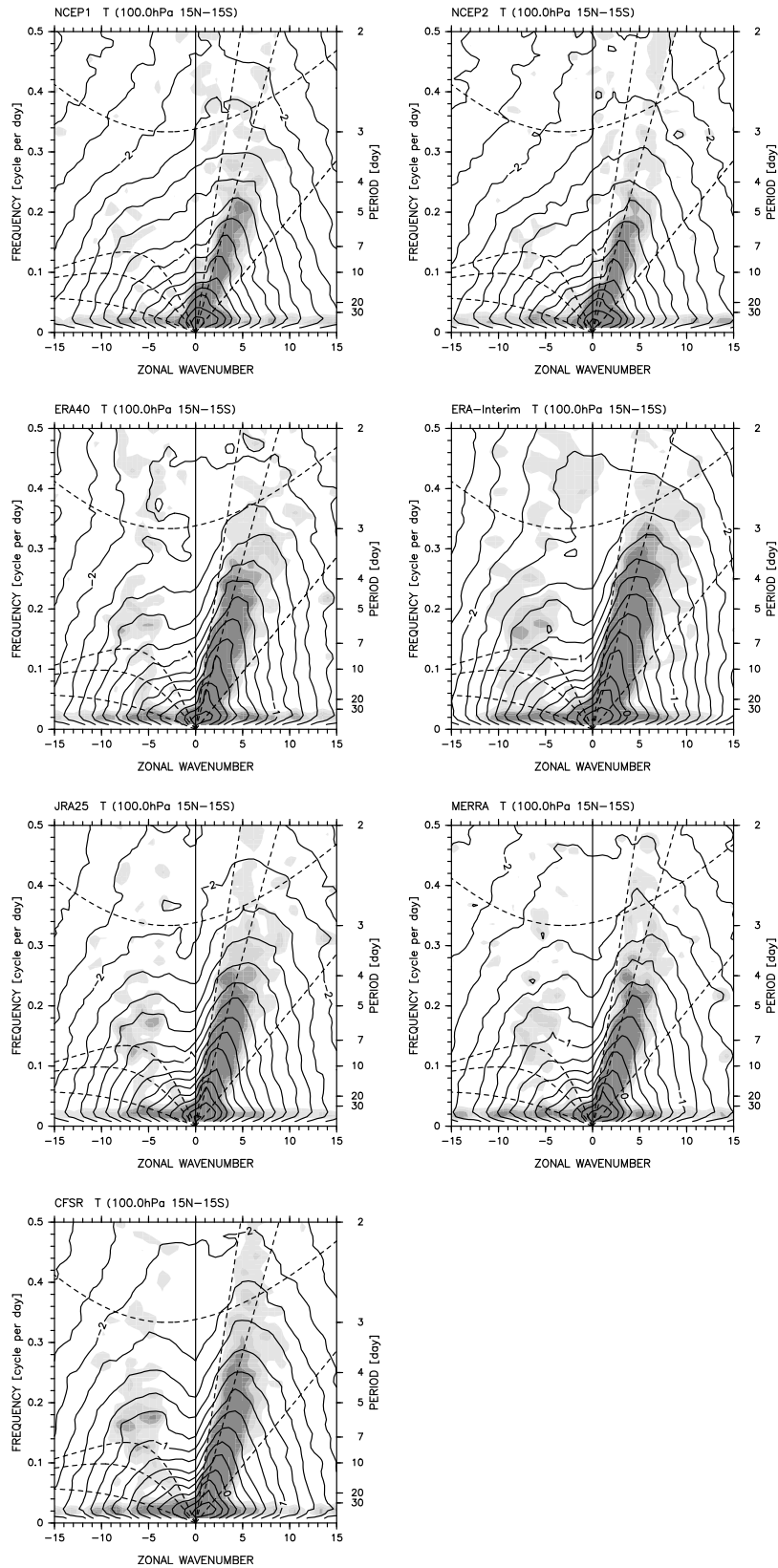


Figure 6

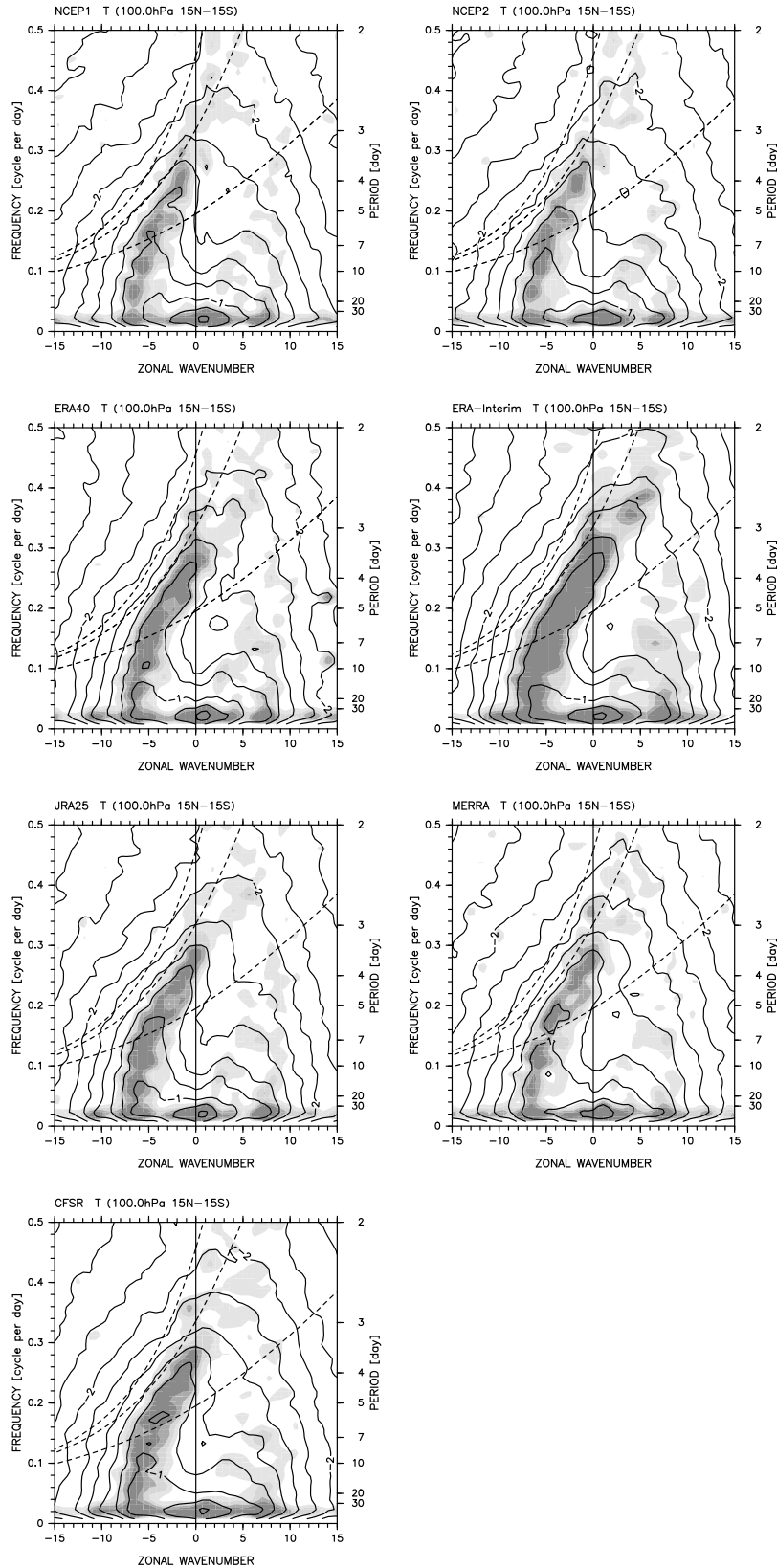


Figure 7. As for Figure 6, but for the antisymmetric component. Dotted curves show the equatorial-wave dispersion relation at $h = 8, 70,$ and 240 m for mixed Rossby-gravity waves (negative wave numbers) and $n = 0$ eastward-moving inertio-gravity waves (positive wave numbers).

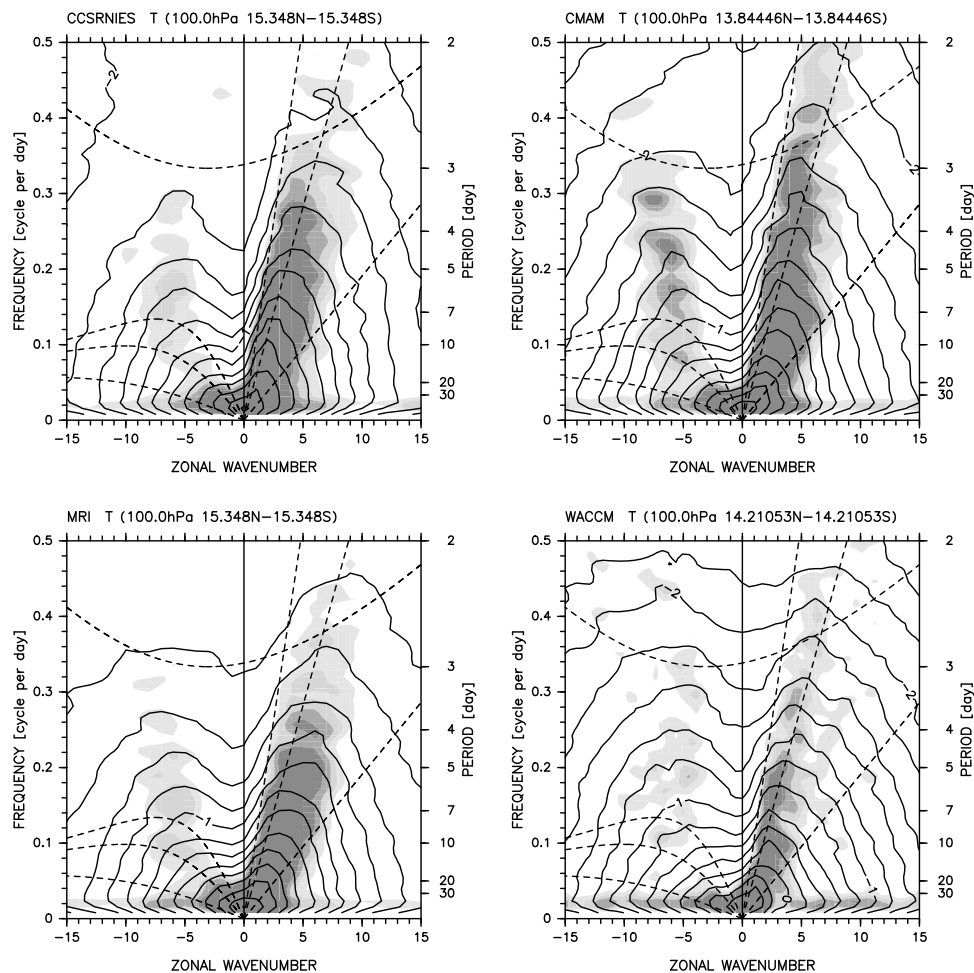


Figure 8. As for Figure 6, but for 4 CCMs.

on the general slope down to higher frequencies and higher zonal wave numbers.

[31] In the symmetric figures for temperature (Figures 6 and 8), we observe a distinct ridge in contours in the positive zonal wave number region, roughly from (zonal wave number 1, frequency 0.05 day^{-1}) to (7, 0.3) for all the 11 data sets; these are equatorial Kelvin waves. The ridge region is colored gray and located within the two dispersion relation lines for Kelvin waves at $h = 8 \text{ m}$ and 240 m . However, the signal strengths are different for different data sets even within the RAs (see the locations of, e.g., 10^{-1} and $10^{-2} \text{ K}^2 \text{ day}$ contour curves); this indicates different wave activity values for different data sets. The gray regions for NCEP1 and NCEP2 are relatively small compared with the other RAs; this is consistent with the contour distribution for these two data sets, with gentler slopes on the higher frequency side. The 4 CCMs show broadly similar contour and gray-tone distributions to those for the RAs other than NCEP1 and NCEP2. The power spectral density values at high frequencies for CCSRNIES and MRI are much greater than those for other data sets. Also, the MJO is observable as a ridge around 0.02 day^{-1} frequency for all the 11 data sets. Finally, we note that equatorial Rossby waves (in the negative zonal wave number region at low frequencies in Figures 2 and 4) are not very obvious in all the 11 data sets.

[32] In the antisymmetric figures for temperature (Figures 7 and 9), we observe a distinct ridge in contours in the negative zonal wave number region, roughly from (zonal wave number -5 , frequency 0.16 day^{-1}) to (0, 0.26) for all the 11 data sets; these are MRG waves. The ridge region is colored gray and located generally within the two dispersion relation curves for MRG waves at $h = 8 \text{ m}$ and 70 m . (We note, however, that the signals extend to the lower frequencies; this might indicate the co-existence of another free Rossby mode [e.g., Madden, 2007]. This is a subject for further investigation in another study.) Again, we observe that the signal strengths (i.e., the contour values) are different for different data sets even within the RAs. We note that the 4 CCMs show relatively strong signals in the positive zonal wave number region at lower frequencies, while the 7 RAs only show very weak signals in the same region. These signals might be equatorial Kelvin waves which propagate along off-equatorial latitudes due to, e.g., equatorially antisymmetric distributions of the background wind and convective heating.

4.2.2. Zonal and Meridional Wind at 100 hPa

[33] Figures 10 and 11 show the spectrum for zonal wind at 100 hPa for the symmetric and antisymmetric component, respectively, from 2 RAs (ERA40 and MERRA) and the 4 CCMs. ERA40 is chosen as the representative of the RA

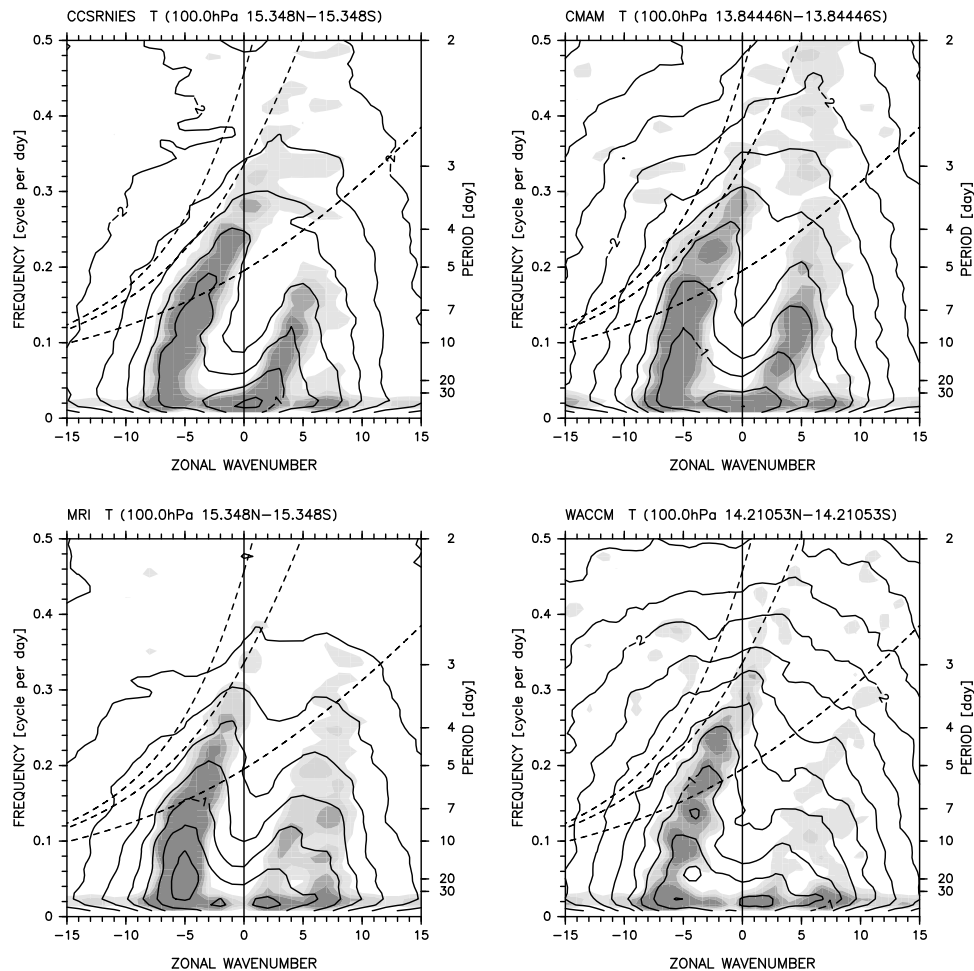


Figure 9. As for Figure 7, but for 4 CCMs.

majority, and MERRA is chosen as the one with larger wave activities, as will be shown in section 4.3.

[34] In the symmetric component (Figure 10), we observe the signals of equatorial Kelvin waves in the similar region as for temperature (Figures 6 and 8). We observe that the signal strengths are somewhat different for different data sets (see, e.g., 10^{+1} (m s^{-1})² day contour curves). Also, the MJO may be observable as a ridge around 0.01 day^{-1} frequency. It should be noted that all the 11 data sets show relatively strong signals evaluated as significant around zonal wave numbers -3 to -5 and at frequencies $< 0.3 \text{ day}^{-1}$. These signals are probably free Rossby waves [e.g., Madden, 2007; Hendon and Wheeler, 2008] and/or MRG waves which propagate along off-equatorial latitudes due to, e.g., equatorially antisymmetric distributions of the background wind and convective heating. The temperature plots (Figures 6 and 8) show very weak signals around the same zonal wave number-frequency region for most of the data sets.

[35] In the antisymmetric component (Figure 11), we observe the signals of MRG waves in the similar region as for temperature (Figures 7 and 9). Again, we observe that the signal strengths are different for different data sets. We also observe signals evaluated as significant in the positive zonal wave number region, along the ridge roughly from (zonal wave number 3, frequency 0.08 day^{-1}) through (5, 0.2) to larger frequencies. These signals are probably in part

representing standing signals and/or Kelvin waves which propagate along off-equatorial latitudes.

[36] ERA40 and MERRA show relatively strong signals around positive zonal wave numbers 13–15 and periods of 7–10 and 4–5 day for both symmetric and antisymmetric components. For these two RAs, similar signals are also found in the temperature spectra (Figures 6 and 7). ERA-Interim also shows these signals though much weaker than ERA40, but the other RAs do not show such distinct signals. These signals are due to the assimilation of radiance/temperature measurements from polar orbital satellites [Wheeler and Kiladis, 1999] as described in section 2.3 for NOAAOLR data. It is inferred that ERA40 and MERRA put larger weight on satellite radiance measurements in the tropics compared with the other RAs and that the artificial signals in temperature has propagated into the wind data through the mass-wind coupling.

[37] For the meridional wind (not shown), the symmetric-antisymmetric decomposition is switched from that for temperature, zonal wind, and OLR. MRG waves and $n = 0$ eastward-moving inertio-gravity waves are categorized as the symmetric component, and the MJO as the antisymmetric component. Note also that Kelvin waves do not have the meridional wind component in the linear wave theory. We observe the signals of MRG waves in the symmetric

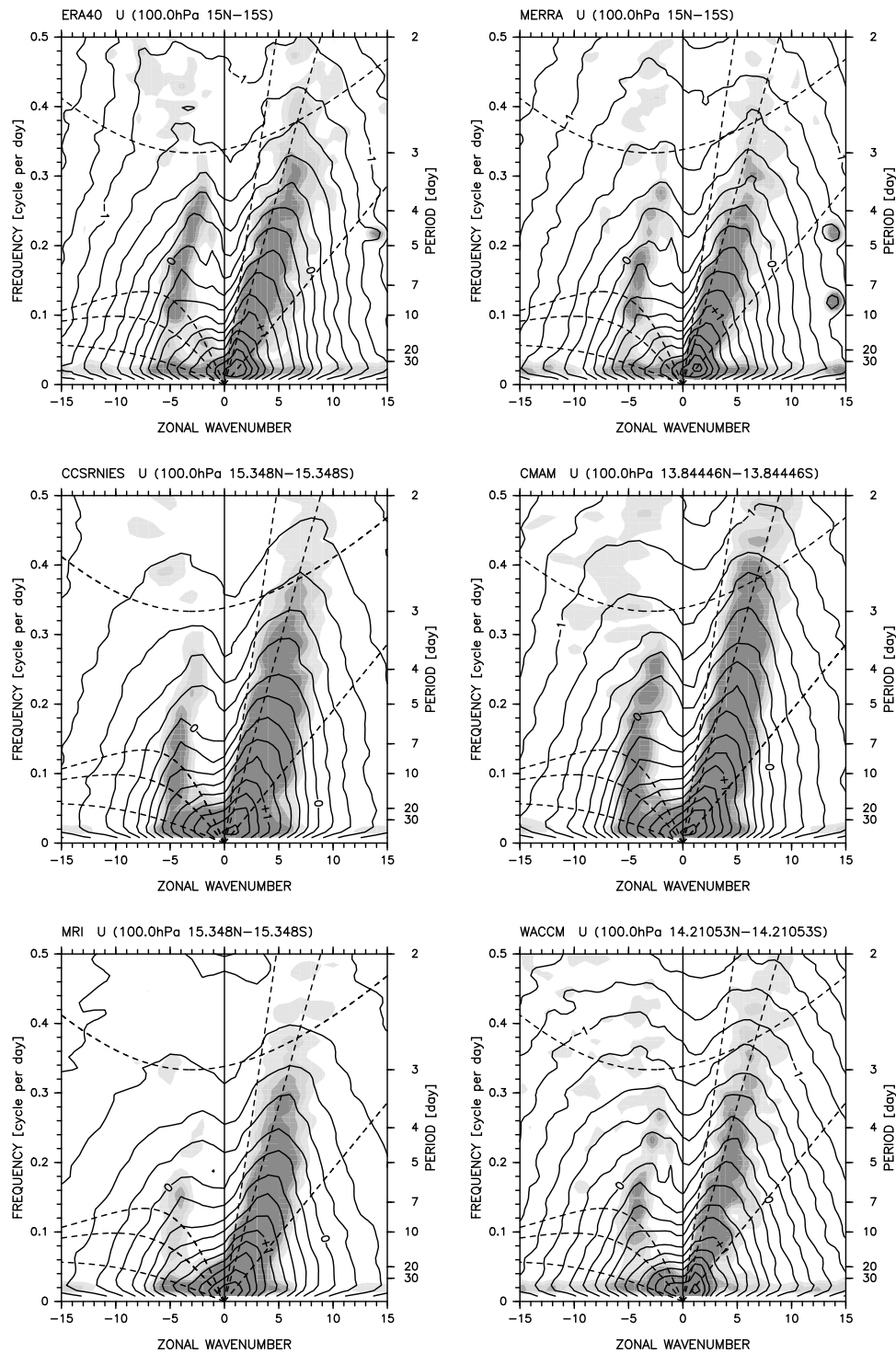


Figure 10. As for Figure 6, but for zonal wind at 100 hPa for 2 RAs (ERA40 and MERRA) and 4 CCMs.

spectrum in the similar region as in the antisymmetric component of temperature and zonal wind (not shown).

4.2.3. OLR

[38] Figures 12 and 13 show the spectrum for OLR for the symmetric and antisymmetric component, respectively, from NOAAOLR and the 4 CCMs. For NOAAOLR, equatorial Kelvin waves, equatorial Rossby waves, the MJO, and MRG waves are identified. For MRG waves, however, the regions evaluated as significant are smaller than those by *Wheeler*

and *Kiladis* [1999]. This is in part because of the different method for constructing the background spectrum; we have confirmed that averaging the smoothed spectra for symmetric and antisymmetric components to obtain a common background spectrum, as was done by *Wheeler and Kiladis* [1999], results in greater significance in the MRG-wave region.

[39] The spectra from the CCMs show very different and much smoother distributions, with only very weak signals

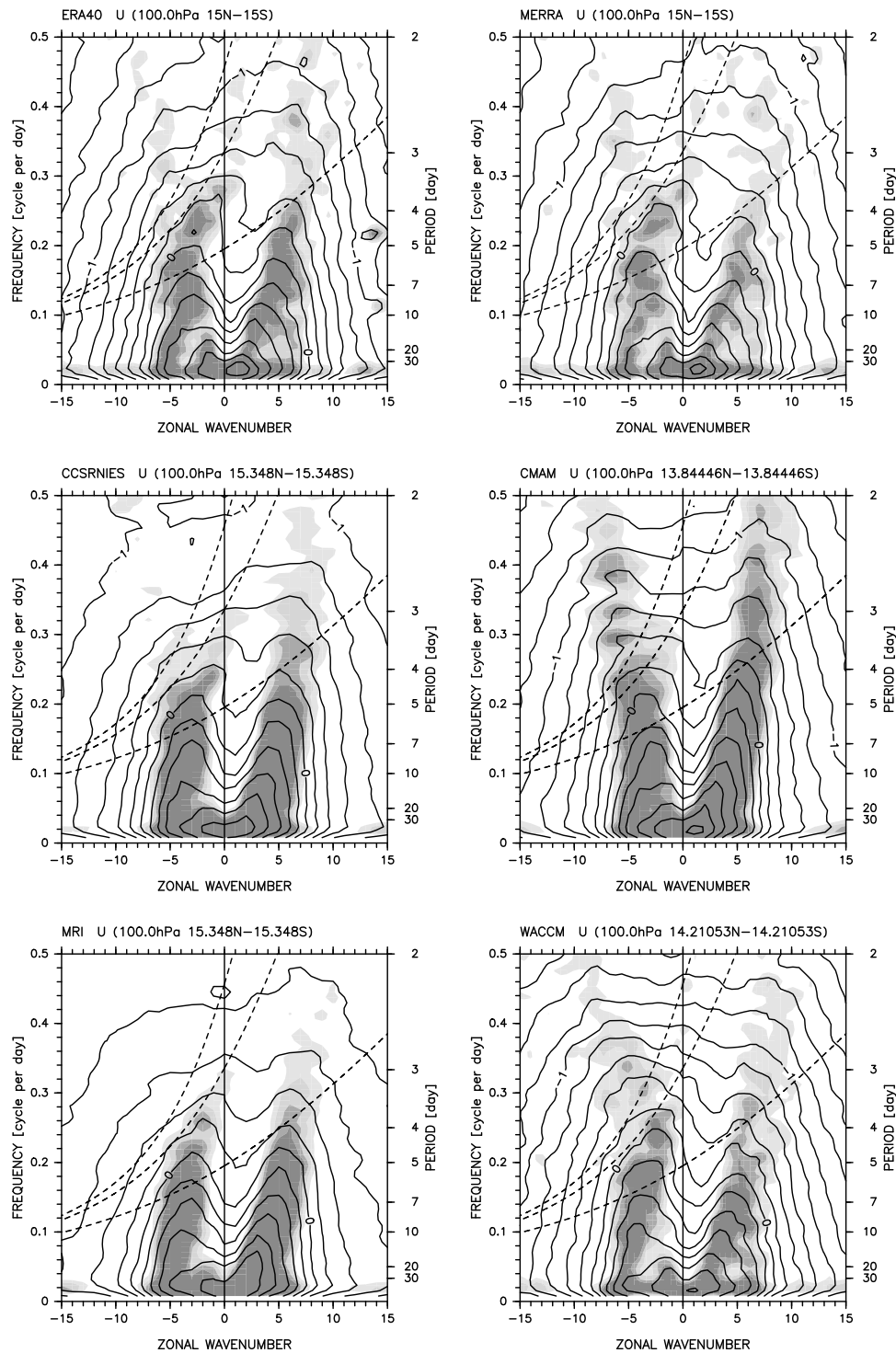


Figure 11. As for Figure 7, but for zonal wind at 100 hPa for 2 RAs (ERA40 and MERRA) and 4 CCMs.

corresponding to the disturbances identified in NOAAOLR data. In the symmetric component (Figure 12), the ridge for Kelvin waves is much broader, and the powers at -5 to -1 zonal wave numbers at $<0.04 \text{ day}^{-1}$ frequencies (i.e., the signals for westward-moving intraseasonal oscillations) are relatively large. In the antisymmetric component (Figure 13), the signals for MRG waves are largely missing, and again, the signals for westward-moving intraseasonal oscillations are relatively large. The longitude-time distribution of OLR

at/near the equator (not shown) confirms that all the CCMs are with much fewer (or largely missing) eastward-moving large-scale disturbances which are observed over the Indian Ocean to the tropical western Pacific at 45°E – 180° longitudes in NOAAOLR data.

[40] A question arises why the CCM temperature and horizontal wind fields at 100 hPa show more realistic features for large-scale disturbances while the CCM OLR field does not. It is inferred that for the large-scale disturbances in

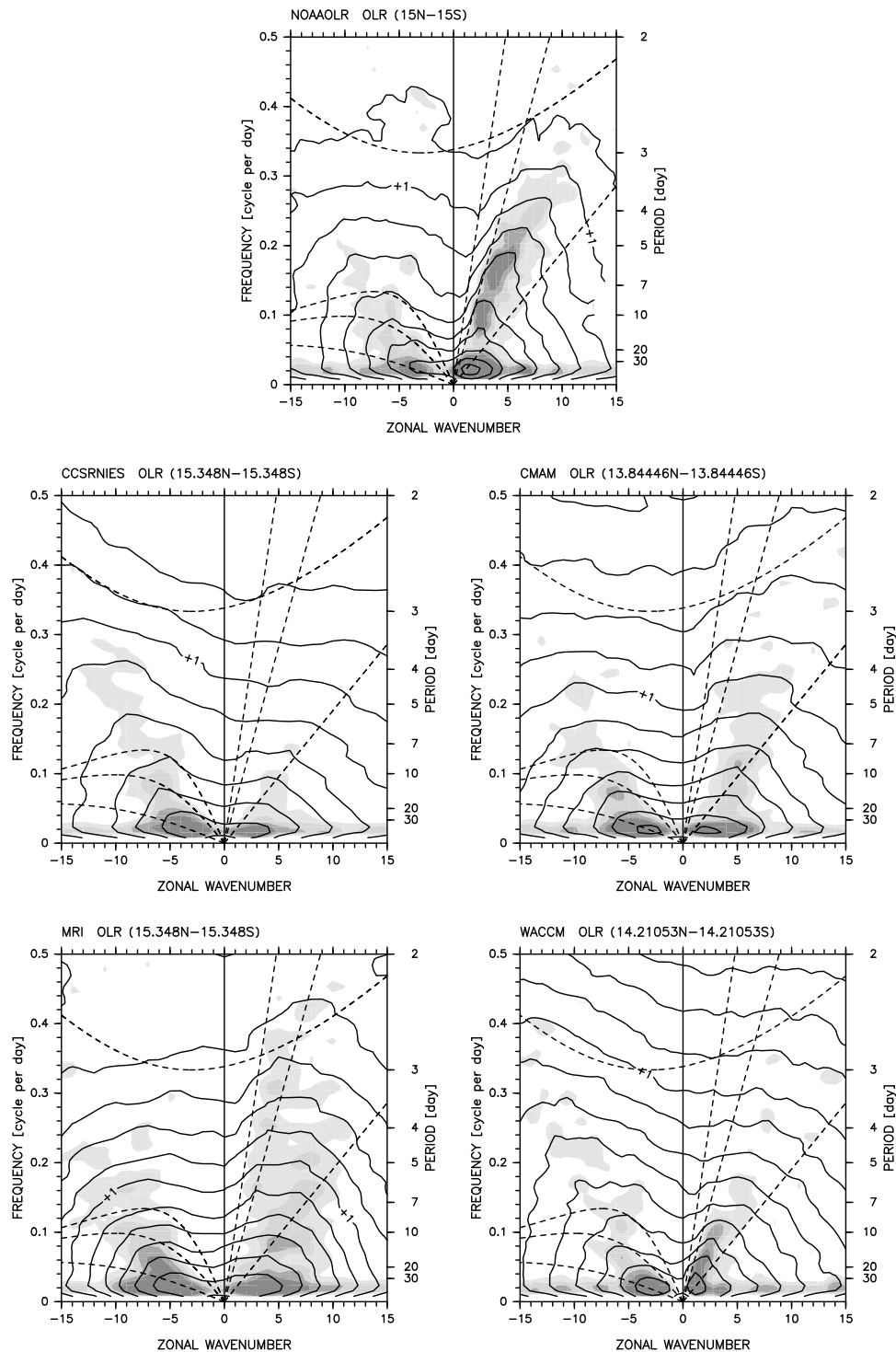


Figure 12. As for Figure 6, but for OLR for NOAAOLR and 4 CCMs. The power values for NOAAOLR at positive zonal wave numbers 13–15 and periods of 7–10 and 4–5 day are flagged as special values (see Section 2.3).

the TTL, the dynamical constraints in the equatorial region (i.e., relevant to the equatorial β plane) may be more important than the *distributions* of diabatic heating associated with tropical organized convection. It is also noted that the precipitation is more directly linked to the wave activity [Horinouchi *et al.*, 2003] and that the OLR is more directly

determined by stratiform clouds (and thus the large-scale condensation processes) which are in many cases detrained from deep convection. Therefore, precipitation and other cloud-related data also need to be analyzed to fully understand the relationship between the cloud activity and wave activity in the CCMs.

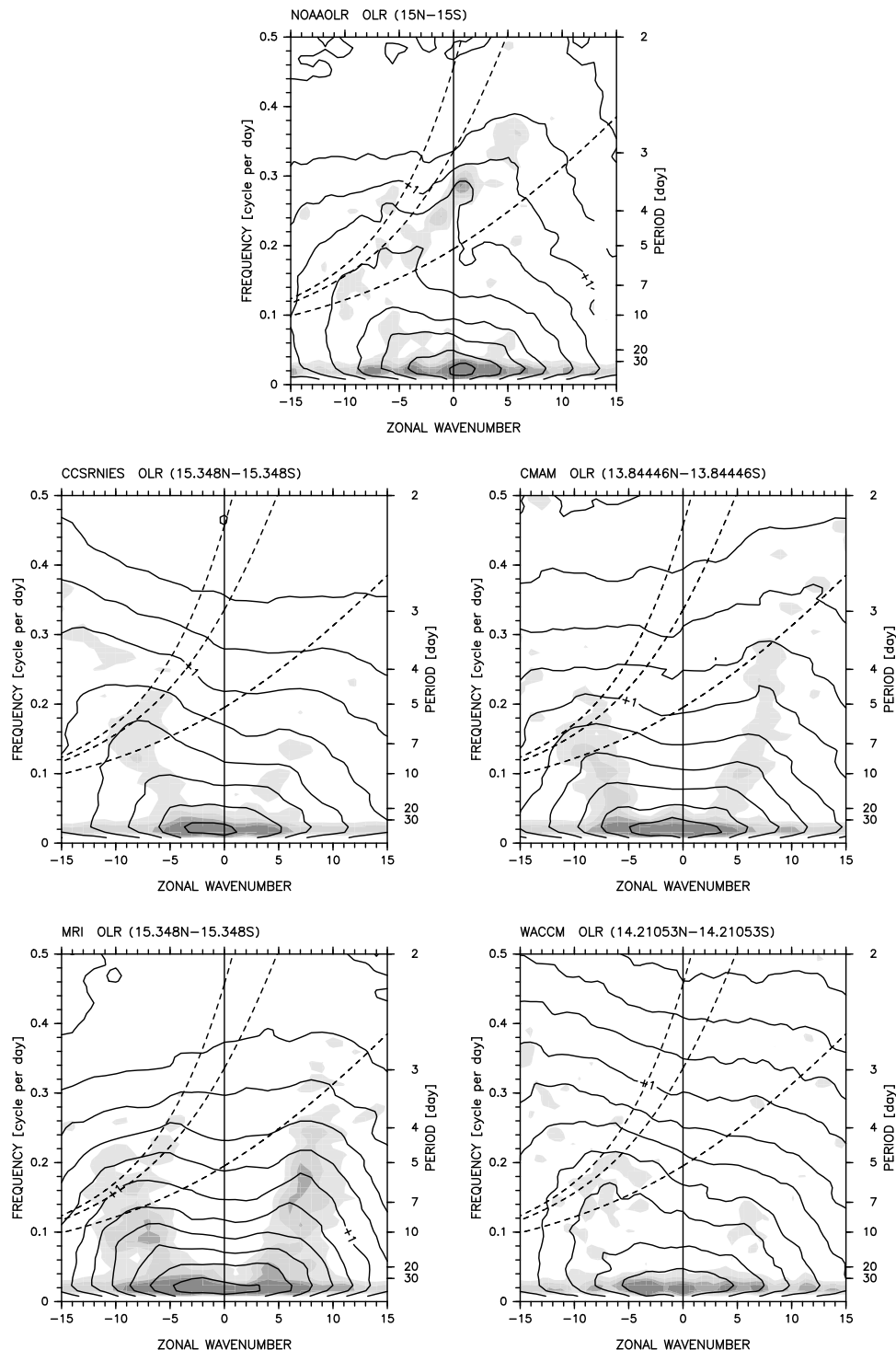


Figure 13. As for Figure 7, but for OLR for NOAAOLR and 4 CCMs. The power values for NOAAOLR at positive zonal wave numbers 13–15 and periods of 7–10 and 4–5 day are flagged as special values (see section 2.3).

4.3. Wave Activity

[41] In this section, the comparison of the activity for Kelvin waves, MRG waves, and the MJO is discussed for the 7 RA, 4 CCM, and NOAAOLR data sets. The activity is defined as the variance, i.e., the power spectral density or the background spectrum integrated in a particular zonal wave

number-frequency region for the total activity or for the background activity, respectively. The (true) wave activity is then obtained by subtracting the background activity from the total activity. In this way, we estimate the wave activity and background activity separately. The integration region is defined as follows. For Kelvin waves, the integration region is zonal wave number 1–10, frequency $0.05\text{--}0.5\text{ day}^{-1}$, and

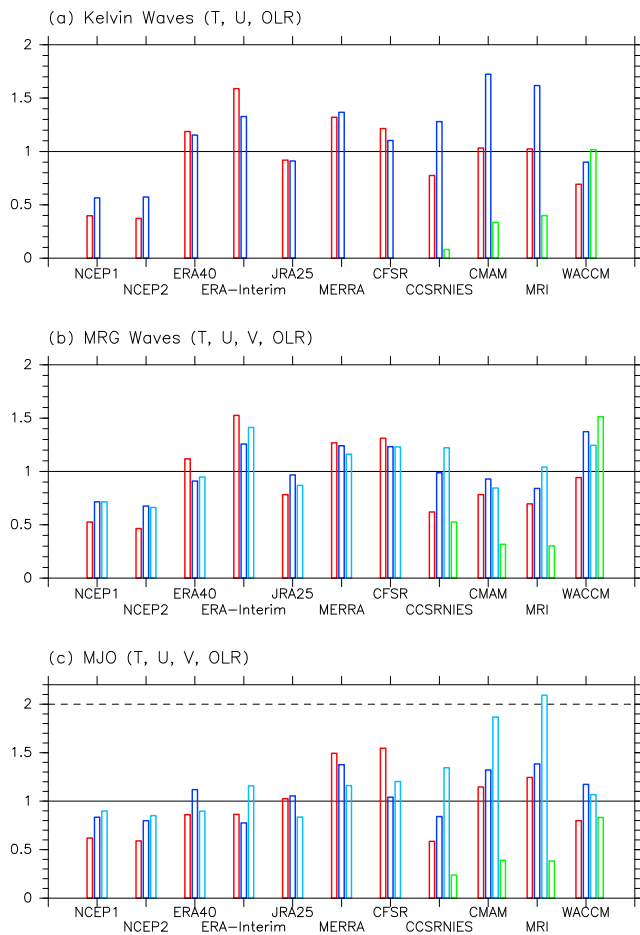


Figure 14. The (true) wave activity shown as the ratio to the average for the 7 RAs (for temperature and horizontal winds) or to the value for NOAAOLR (for OLR) for (a) Kelvin waves, (b) MRG waves, and (c) MJO for 7 RAs and 4 CCMs. See Table 3 for the RA average values and NOAAOLR values. Red bars are for temperature at 100 hPa, dark blue for zonal wind at 100 hPa, light blue for meridional wind at 100 hPa, and green for OLR. See text for the definition of the activity for each disturbance.

h 8–240 m for the symmetric component of temperature, zonal wind, and OLR. For MRG waves, the integration region is zonal wave number -10 to 0 and h 8–70 m for the antisymmetric component of temperature, zonal wind, and OLR and for the symmetric component of meridional wind. (Note again that another free Rossby mode might be superimposed; see section 4.2.1.) For the MJO, the integration region is zonal wave number $1-5$ and frequency $0-0.05 \text{ day}^{-1}$ for the symmetric component of temperature, zonal wind, and

Table 3. Wave Activities Averaged for the 7 RAs and From the NOAAOLR

| Parameter | Unit | Kelvin Waves | MRG Waves | MJO |
|---------------------------|-----------------------|--------------|-----------|------|
| Temperature (100 hPa) | K^2 | 0.11 | 0.0096 | 0.12 |
| Zonal wind (100 hPa) | $(\text{m s}^{-1})^2$ | 1.6 | 0.13 | 3.0 |
| Meridional wind (100 hPa) | $(\text{m s}^{-1})^2$ | – | 0.45 | 0.15 |
| OLR (NOAA) | $(\text{W m}^{-2})^2$ | 8.8 | 1.3 | 20 |

OLR and for the antisymmetric component of meridional wind. For all the three disturbances, the statistical significance information (i.e., the regions colored gray in the spectrum figures) is *not* considered during the integration; this does not affect the (true) wave activity estimation because the components from the statistically insignificant regions are largely canceled out during the subtraction. It is also noted that the background spectrum estimated with the many passes of 1-2-1 filter may still contain some wave signals [Wheeler and Kiladis, 1999]; therefore, the obtained (true) wave activity is regarded as the lower limit.

[42] Figure 14 summarizes the wave activities shown as the ratio to those averaged for the 7 RAs, or to the values from the NOAAOLR for the case of OLR. The reference wave activity values are summarized in Table 3, which shows that in general, the MJO variances are similar to or a factor of ~ 2 greater than the Kelvin wave variances for all the relevant parameters, while the MRG wave variances are much smaller for the parameters except for meridional wind.

[43] Figure 14 shows that Kelvin wave variances in the RAs are about half of the RA average in NCEP1 and NCEP2, similar to the average in JRA25, ERA40, and CFSR, ~ 1.3 in MERRA, and 1.3–1.6 in ERA-Interim. Kelvin wave variances in the CCMs show different tendencies for different parameters: For temperature at 100 hPa, the variances are 0.7–0.8 in CCSRNIES and WACCM, and

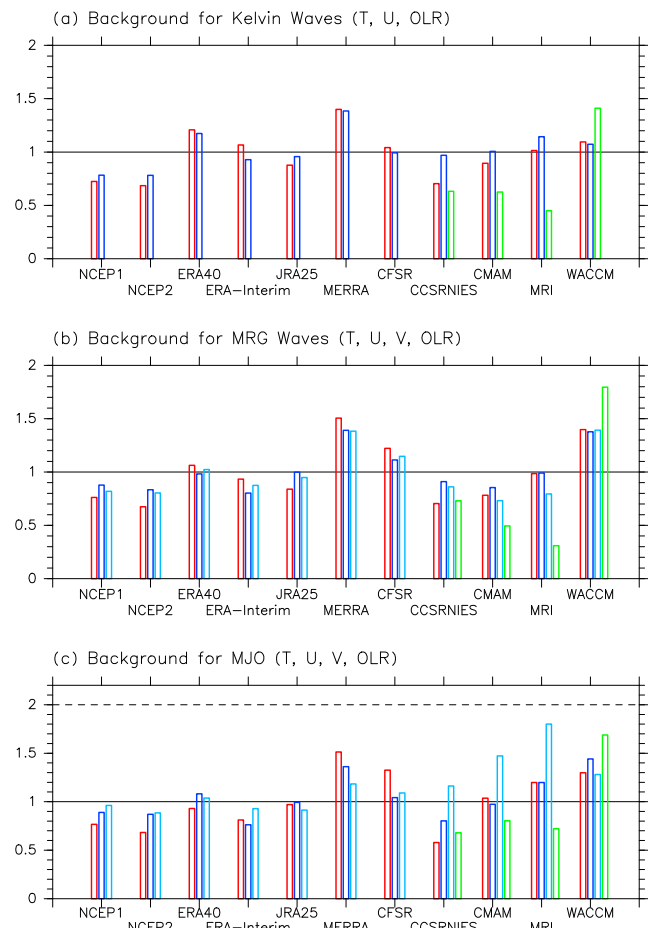


Figure 15. As for Figure 14, but for the background activity. See Table 4 for the RA average values and NOAAOLR values.

Table 4. Background Activities Averaged for the 7 RAs and From the NOAAOLR

| Parameter | Unit | Kelvin Waves | MRG Waves | MJO |
|---------------------------|-----------------------------------|--------------|-----------|------|
| Temperature (100 hPa) | K ² | 0.20 | 0.030 | 0.14 |
| Zonal wind (100 hPa) | (m s ⁻¹) ² | 2.9 | 0.47 | 2.4 |
| Meridional wind (100 hPa) | (m s ⁻¹) ² | – | 0.89 | 0.24 |
| OLR (NOAA) | (W m ⁻²) ² | 51 | 16 | 25 |

similar in CMAM and MRI; for zonal wind at 100 hPa, the variances are ~ 0.9 in WACCM and 1.3–1.7 in the other three CCMs; and for OLR, the variances are only ~ 0.1 of the NOAAOLR value in CCSRNIES, 0.3–0.4 in CMAM and MRI, and similar in WACCM.

[44] MRG wave variances in the RAs are ~ 0.6 of the RA average in NCEP1 and NCEP2, similar to the average in ERA40 and JRA25, ~ 1.3 in MERRA and CFSR, and 1.3–1.5 in ERA-Interim. MRG wave variances in the CCMs show different tendencies for different parameters: For temperature, the variances are 0.6–0.8 in CCSRNIES, CMAM, and MRI, and similar in WACCM; for horizontal winds, the variances are similar in CCSRNIES, CMAM, and MRI, and 1.2–1.4 in WACCM; and for OLR, the variances are ~ 0.3 of the NOAAOLR value in CMAM and MRI, ~ 0.5 in CCSRNIES, and ~ 1.5 in WACCM.

[45] The MJO in the RAs are 0.6–0.9 of the RA average in NCEP1 and NCEP2, similar to the average in ERA40, ERA-Interim, and JRA25, and 1.0–1.6 in MERRA and CFSR. The MJO variances in the CCMs show different tendencies for different parameters: For temperature and zonal wind, the variances are 0.6–0.8 in CCSRNIES, 0.8–1.2 in WACCM, and 1.2–1.4 in CMAM and MRI; for meridional wind, the variances are similar in WACCM, ~ 1.3 in CCSRNIES, and ~ 2.0 in CMAM and MRI; and for OLR, the variances are 0.2–0.4 of the NOAAOLR value in CCSRNIES, CMAM, and MRI, and ~ 0.8 in WACCM.

[46] Figure 15 and Table 4 summarize the background activities. Table 4 shows that the background activity is greater than the (true) wave activity for all the three disturbances and for all the parameters investigated. These background activity values are considered as the upper limit because of the margin for the defined integration regions and possible, remaining wave signals in the background spectra. Figures 14 and 15 show that the relative relationship among the data sets is quite similar between the wave activity and the background activity. Some marked differences include the following points: (1) ERA-Interim has large wave activities for Kelvin and MRG waves but moderate background activities for them; and (2) the background activities for the CCMs show smaller parameter-to-parameter differences particularly for Kelvin waves.

[47] As described in section 2.1, the RAs are constructed using various observations with an assimilation scheme and a global forecast model. The observational data relevant to the TTL region during the period of 1990–2000 are radiosonde data and satellite radiance-based data. Also, wind data from tracking of features in geostationary satellite images are available for the lower TTL region. Note that the GPS radio occultation temperature data, which are of high quality with a comprehensive coverage in the TTL, were not available during this period. It is unclear whether the detailed

procedures how to incorporate available data into each RA have resulted in the wave activity difference among the RAs shown in Figures 14 and 15. It is also noted that for satellite radiance-based data, retrieved temperature data are assimilated in NCEP1 and NCEP2 [Kalnay *et al.*, 1996], while raw radiance data are assimilated in the other RAs [e.g., Uppala *et al.*, 2005; Saha *et al.*, 2010; D. Dee, private communication, 2011]; but this may not have a direct relevance to the difference in sub-seasonal variability amplitudes. The assimilation schemes relevant to this study are 4D-Var for ERA-Interim and 3D-Var for all the other RAs. The result that ERA40 and ERA-Interim show different wave activity values for Kelvin and MRG waves suggests that the difference between 3D-Var and 4D-Var may have some contributions to the difference in the obtained wave activities. The global forecast model itself has several components, but the vertical resolution in the TTL can have a major contribution because the vertical wavelengths of the disturbances in the TTL are relatively short, e.g., 2.5–5.6 km for the case of Kelvin waves shown in Figure 5 [Fujiwara *et al.*, 1998]. In fact, NCEP1 and NCEP2 have ~ 2 km resolution, while all the other RAs have ~ 1 km resolution (Table 1). The lower vertical resolution in NCEP1 and NCEP2 may be the primary reason for the lower wave and background activities in the TTL.

[48] The wave and background activities in the CCMs for the parameters at 100 hPa lie generally within the range of the RA results, with some exceptions in horizontal winds. Different tendencies for different parameters are observed in the CCMs. This might indicate the inconsistency in the RAs instead, as well as the fact that the mass-wind coupling is weak in the tropics. For OLR, the wave activities are too low in CCSRNIES, CMAM, and MRI, and the background activities are too high in WACCM, for all the three disturbances. It is noted again that CMAM and WACCM use the Zhang-McFarlane scheme for the cumulus parameterization, and CCSRNIES and MRI use a prognostic Arakawa-Schubert scheme (though the radiation calculation in MRI is made at lower resolution). The difference in the OLR is not simply explained by the choice of the cumulus parameterization scheme; investigation is also necessary for the detailed parameter setting for the cumulus scheme and for the large-scale condensation scheme. As already shown in Figures 12 and 13, the large-scale wave realization in the tropical OLR in all the 4 CCMs are quite different from the observations and need to be improved in the future.

[49] In summary, there is a general tendency within the 7 RAs that NCEP1 and NCEP2 exhibit smallest, ERA40 and JRA25 medium, and ERA-Interim, MERRA, and CFSR largest large-scale wave activity in the TTL. The smallest activity in NCEP1 and NCEP2 is probably due to the low TTL vertical resolution of their forecast model. The TTL large-scale wave activity in the 4 CCMs is generally within the range of that in the 7 RAs. The wave activity in the OLR is much smaller in CCSRNIES, CMAM, and MRI, and the background activity is much greater in WACCM, than those observed in the NOAAOLR, though the reason for this behavior is unclear.

5. Summary and Concluding Remarks

[50] We investigated the activity of equatorial Kelvin waves, MRG waves, and the MJO in the TTL by using the

Table A1. Resolution and Number of 1-2-1 Filter Passes for Zonal Wave Number for Each Data Set

| Data Set | MX | MMX | Resolution (MX/MMX) | Number of Passes |
|-------------|-----|------|---------------------|------------------|
| NOAAOLR | 144 | 256 | 0.5625 | 40 |
| NCEP1 | 144 | 256 | 0.5625 | 40 |
| NCEP2 | 144 | 256 | 0.5625 | 40 |
| ERA40 | 144 | 256 | 0.5625 | 40 |
| ERA-Interim | 240 | 256 | 0.9375 | 24 |
| JRA25 | 288 | 512 | 0.5625 | 40 |
| MERRA | 540 | 1024 | 0.52734375 | 43 |
| CFSR | 720 | 1024 | 0.703125 | 32 |
| CCSRNIES | 128 | 128 | 1.0 | 23 |
| CMAM | 64 | 64 | 1.0 | 23 |
| MRI | 128 | 128 | 1.0 | 23 |
| WACCM | 144 | 256 | 0.5625 | 40 |

zonal wave number-frequency spectral analysis method with equatorially symmetric-antisymmetric decomposition. Comparisons were made for data from 7 RAs (NCEP1, NCEP2, ERA40, ERA-Interim, JRA25, MERRA, and CFSR) and 4 CCMs (CCSRNIES, CMAM, MRI, and WACCM), with the original motivation to validate CCMs. Because the spatial and temporal resolutions vary for these data sets, careful considerations were made for the background spectrum estimation to allow for fair comparison.

[51] The basic comparisons for the climatology and inter-annual variations of tropical 100 hPa temperature showed that different RAs show different results that are significant for the quantitative understanding of the dehydration processes in the TTL; the 4 CCMs show much greater variety in this regard and basically do not reproduce the interannual variations with ≥ 3 -year timescales. A large-amplitude Kelvin wave case over Indonesia in May–June 1995 suggested that the large-scale wave activity could be different for different RAs with much smaller activity for NCEP1 and NCEP2 and probably larger activity for MERRA.

[52] Spectral analysis was performed for temperature and horizontal winds at 100 hPa for the 7 RAs and 4 CCMs and for OLR for the NOAAOLR and 4 CCMs. Equatorial Kelvin waves, MRG waves, and the MJO were identified from all the data sets at 100 hPa. We found that the spectrum for OLR in the CCMs is very different compared to that obtained from observations, with much smoother distributions, while the spectra for the other parameters in the TTL in the CCMs show wave signals corresponding to those shown in the RAs very well. This might be contradictory because the large-scale waves in the TTL are basically generated by large-scale organized convective systems in the tropics [e.g., Fujiwara and Takahashi, 2001; Suzuki *et al.*, 2010b]. This could be due to much stronger constraints by equatorial wave dynamics than those by the *distributions* of diabatic heating determined by the large-scale organized convection in the tropics. Precipitation and other cloud-related data also need to be analyzed to fully understand the relationship between the cloud activity and wave activity in the CCMs.

[53] The wave activity and the corresponding background activity were then defined and calculated for Kelvin waves, MRG waves, and the MJO, and shown with respect to the RA averages for temperature and horizontal winds at tropical 100 hPa and with respect to the NOAAOLR values for OLR.

It was found that there is a general tendency within the 7 RAs that NCEP1 and NCEP2 exhibit smallest, ERA40 and JRA25 medium, and ERA-Interim, MERRA, and CFSR largest large-scale wave activity in the TTL; in other words, the newer RAs show larger wave activity. The results from the 4 CCMs in the TTL were found to lie generally within the range of those obtained from the 7 RAs. It was also found that the wave activity in the OLR is much smaller in CCSRNIES, CMAM, and MRI, and the background activity is much greater in WACCM, than in the NOAAOLR.

[54] This study has revealed that newer RAs (other than NCEP1 and NCEP2) still show different tropical tropopause temperature values even for the climatology. We note again that a 1 K temperature difference at 100 hPa roughly corresponds to ~ 1 ppmv saturation water vapor mixing ratio difference [Fujiwara *et al.*, 2010] and that a water vapor change in the lower stratosphere of this magnitude can have a significant effect on surface temperatures [Solomon *et al.*, 2010]. The large-scale wave activity statistics in the TTL showed significant differences between the different RAs with a range between ~ 0.7 and ~ 1.4 with respect to the RA averages. The smallest activity in NCEP1 and NCEP2 is probably due to the low TTL vertical resolution of the forecast model. The large activity in ERA-Interim, MERRA, and CFSR may be too large, and as a result, the ensemble of RA wave activities may be about right. But, further studies are necessary to validate the RAs by, e.g., statistically comparing with research satellite data sets and research radiosonde data sets that are not included in the RA procedure and thus are independent of the RA products.

[55] The large-scale wave activity in the TTL obtained from the 4 CCMs was found to lie generally within the range of that from the 7 RAs, with some exceptions. However, given the uncertainty in the RAs' activity, this does not mean that the CCMs show realistic results; at least, the tropical OLR variability in the 4 CCMs did not resemble that of the NOAAOLR data set. Improvements in the observational data base is needed in order to obtain better constraints on model-measurement intercomparisons. It is suggested that our understanding of the processes controlling the wave activity in the TTL is still not sufficient.

Appendix A: Number of 1-2-1 Filter Passes for Background Spectrum Estimation

[56] We set the number of 1-2-1 filter passes for each data set so as to be inversely proportional to the number of passes for the NOAAOLR data set (10 in frequency and 40 in zonal wave number) according to the wave number/frequency resolution. The wave number/frequency resolution depends on both the spatial/temporal resolution of the data and the array size for the fast Fourier transform routine, MMX for zonal direction and MMT for time. MMX and MMT are 2^n where n is integer, and satisfy the following relation, $MX \leq MMX < MX \times 2$, and $MT \leq MMT < MT \times 2$, where MX is the number of data in zonal direction (e.g., $MX = 360/2.5 = 144$ for the data sets with a 2.5° resolution) and MT is the number of data in time (i.e., MT is 92 for daily data sets and 92×4 for four-times-daily data sets). Table A1 summarizes the resolution and the number of passes for zonal wave number for each data set. The zonal wave number resolution is calculated from MX/MMX. The number of

passes for frequency becomes 10 for both daily data set (the temporal resolution, $DT = 1$, and $MMT = 128$) and four-times-daily data set ($DT = 1/4$ and $MMT = 128 \times 4$) because the frequency resolution, $1/(MMT \times DT)$, is 0.0078125 for both.

[57] **Acknowledgments.** The CCSRNIES research was supported by the Global Environmental Research Fund of the Ministry of the Environment of Japan (A-071 and A-0903). The CCSRNIES and MRI simulations were made with the supercomputer at the National Institute for Environmental Studies, Japan. The CMAM simulations were made at Environment Canada, and generously supported by the Canadian Foundation for Climate and Atmospheric Sciences (CFCAS) and the Canadian Space Agency through the C-SPARC program. The National Center for Atmospheric Research (NCAR) is sponsored by the United States National Science Foundation. The NCEP1 and NCEP2 reanalysis data were provided by the NOAA/OAR/ESRL PSD. The ERA40 and ERA-Interim data were provided by the ECMWF through their website (the ERA40 data were actually obtained through an authorized website at RISH, Kyoto University, Japan). The JRA25 data were provided by the JMA and CRIEPI. The MERRA data were provided by NASA/GSFC/GMAO. The NCEP-CFSR data were provided through NOAA/NCDC. The radiosonde data at Bandung, Indonesia were provided by Toshitaka Tsuda at RISH, Kyoto University, Japan. This study was financially supported in part by the Japanese Ministry of Education, Culture, Sports, Science and Technology (MEXT) through Grants-in-Aid for Scientific Research (19740283). Part of this study was made while the first author stayed at NCAR/ACD in 2010. We thank Noriyuki Nishi, M. Joan Alexander, Takatoshi Sakazaki, Yoshio Kawatani, and Takeshi Horinouchi for valuable discussion. We also thank George Kiladis and two anonymous reviewers for valuable comments. Figures 1–15 were produced using the GFD-DENNOU Library.

References

- Akiyoshi, H., L. B. Zhou, Y. Yamashita, K. Sakamoto, M. Yoshiki, T. Nagashima, M. Takahashi, J. Kurokawa, M. Takigawa, and T. Imamura (2009), A CCM simulation of the breakup of the Antarctic polar vortex in the years 1980–2004 under the CCMVal scenarios, *J. Geophys. Res.*, *114*, D03103, doi:10.1029/2007JD009261.
- Alexander, M. J., and D. A. Orland (2010), Equatorial waves in High Resolution Dynamics Limb Sounder (HIRDLS) data, *J. Geophys. Res.*, *115*, D24111, doi:10.1029/2010JD014782.
- Alexander, S. P., T. Tsuda, Y. Kawatani, and M. Takahashi (2008), Global distribution of atmospheric waves in the equatorial upper troposphere and lower stratosphere: COSMIC observations of wave mean flow interactions, *J. Geophys. Res.*, *113*, D24115, doi:10.1029/2008JD010039.
- Boehm, M. T., and J. Verlinde (2000), Stratospheric influence on upper tropospheric tropical cirrus, *Geophys. Res. Lett.*, *27*(19), 3209–3212, doi:10.1029/2000GL011678.
- Chao, W. C., B. Yang, and X. Fu (2008), A revised method of presenting wavenumber-frequency power spectrum diagrams that reveals the asymmetric nature of tropical large-scale waves, *Clim. Dyn.*, *33*(6), 843–847, doi:10.1007/s00382-008-0494-3.
- Dec, D. P., et al. (2011), The ERA-Interim reanalysis: Configuration and performance of the data assimilation system, *Q. J. R. Meteorol. Soc.*, *137*, 553–597, doi:10.1002/qj.828.
- Eguchi, N., and M. Shiotani (2004), Intraseasonal variations of water vapor and cirrus clouds in the tropical upper troposphere, *J. Geophys. Res.*, *109*, D12106, doi:10.1029/2003JD004314.
- Eyring, V., T. G. Shepherd, and D. W. Waugh (Eds.) (2010), SPARC CCMVal report on the evaluation of chemistry-climate models, *SPARC Rep. 5*, World Meteorol. Soc., Geneva, Switzerland.
- Flannaghan, T. J., and S. Fueglistaler (2011), Kelvin waves and shear-flow turbulent mixing in the TTL in (re-)analysis data, *Geophys. Res. Lett.*, *38*, L02801, doi:10.1029/2010GL045524.
- Fueglistaler, S., A. E. Dessler, T. J. Dunkerton, I. Folkens, Q. Fu, and P. W. Mote (2009), Tropical tropopause layer, *Rev. Geophys.*, *47*, RG1004, doi:10.1029/2008RG000267.
- Fujiwara, M., and M. Takahashi (2001), Role of the equatorial Kelvin wave in stratosphere-troposphere exchange in a general circulation model, *J. Geophys. Res.*, *106*(D19), 22,763–22,780.
- Fujiwara, M., K. Kita, and T. Ogawa (1998), Stratosphere-troposphere exchange of ozone associated with the equatorial Kelvin wave as observed with ozonesondes and rawinsondes, *J. Geophys. Res.*, *103*(D15), 19,173–19,182.
- Fujiwara, M., F. Hasebe, M. Shiotani, N. Nishi, H. Vömel, and S. J. Oltmans (2001), Water vapor control at the tropopause by equatorial Kelvin waves observed over the Galápagos, *Geophys. Res. Lett.*, *28*(16), 3143–3146.
- Fujiwara, M., M. K. Yamamoto, H. Hashiguchi, T. Horinouchi, and S. Fukao (2003), Turbulence at the tropopause due to breaking Kelvin waves observed by the Equatorial Atmosphere Radar, *Geophys. Res. Lett.*, *30*(4), 1171, doi:10.1029/2002GL016278.
- Fujiwara, M., et al. (2009), Cirrus observations in the tropical tropopause layer over the western Pacific, *J. Geophys. Res.*, *114*, D09304, doi:10.1029/2008JD011040.
- Fujiwara, M., et al. (2010), Seasonal to decadal variations of water vapor in the tropical lower stratosphere observed with balloon-borne cryogenic frostpoint hygrometers, *J. Geophys. Res.*, *115*, D18304, doi:10.1029/2010JD014179.
- Garcia, R. R., D. R. Marsh, D. E. Kinnison, B. A. Boville, and F. Sassi (2007), Simulation of secular trends in the middle atmosphere, 1950–2003, *J. Geophys. Res.*, *112*, D09301, doi:10.1029/2006JD007485.
- Gettelman, A., et al. (2010), Multimodel assessment of the upper troposphere and lower stratosphere: Tropics and global trends, *J. Geophys. Res.*, *115*, D00M08, doi:10.1029/2009JD013638.
- Gill, A. E. (1980), Some simple solutions for heat-induced tropical circulation, *Q. J. R. Meteorol. Soc.*, *106*, 447–462.
- Gilman, D. L., F. J. Fuglister, and J. M. Mitchell Jr. (1963), On the power spectrum of “red noise,” *J. Atmos. Sci.*, *20*, 182–184.
- Hatsushika, H., and K. Yamazaki (2003), Stratospheric drain over Indonesia and dehydration within the tropical tropopause layer diagnosed by air parcel trajectories, *J. Geophys. Res.*, *108*(D19), 4610, doi:10.1029/2002JD002986.
- Hendon, H. H., and M. C. Wheeler (2008), Some space-time spectral analyses of tropical convection and planetary-scale waves, *J. Atmos. Sci.*, *65*, 2936–2948, doi:10.1175/2008JAS2675.1.
- Highwood, E. J., and B. J. Hoskins (1998), The tropical tropopause, *Q. J. R. Meteorol. Soc.*, *124*, 1579–1604.
- Horinouchi, T., et al. (2003), Tropical cumulus convection and upward-propagating waves in middle-atmospheric GCMs, *J. Atmos. Sci.*, *60*, 2765–2782.
- Immler, F., K. Krüger, M. Fujiwara, G. Verver, M. Rex, and O. Schrems (2008), Correlation between equatorial Kelvin waves and the occurrence of extremely thin ice clouds at the tropical tropopause, *Atmos. Chem. Phys.*, *8*, 4019–4026.
- Iwasaki, T., H. Hamada, and K. Miyazaki (2009), Comparisons of Brewer-Dobson circulations diagnosed from reanalyses, *J. Meteorol. Soc. Jpn.*, *87*(6), 997–1006, doi:10.2151/jmsj.87.997.
- Kalnay, E., et al. (1996), The NCEP/NCAR 40-year reanalysis project, *Bull. Am. Meteorol. Soc.*, *77*(3), 437–471.
- Kanamitsu, M., W. Ebisuzaki, J. Woollen, S.-K. Yang, J. J. Hnilo, M. Fiorino, and G. L. Potter (2002), NCEP-DEO AMIP-II reanalysis (R-2), *Bull. Am. Meteorol. Soc.*, *83*(11), 1631–1643.
- Kiladis, G. N., K. H. Straub, G. C. Reid, and K. S. Gage (2001), Aspects of interannual and intraseasonal variability of the tropopause and lower stratosphere, *Q. J. R. Meteorol. Soc.*, *127*, 1961–1983.
- Kiladis, G. N., K. H. Straub, and P. T. Haertel (2005), Zonal and vertical structure of the Madden-Julian Oscillation, *J. Atmos. Sci.*, *62*, 2790–2809.
- Kiladis, G. N., M. C. Wheeler, P. T. Haertel, K. H. Straub, and P. E. Roundy (2009), Convectively coupled equatorial waves, *Rev. Geophys.*, *47*, RG2003, doi:10.1029/2008RG000266.
- Kistler, R., et al. (2001), The NCEP-NCAR 50-year reanalysis: Monthly means CD-ROM and documentation, *Bull. Am. Meteorol. Soc.*, *82*(2), 247–267.
- Liebmann B., and C. A. Smith (1996), Description of a complete (interpolated) outgoing longwave radiation dataset, *Bull. Am. Meteorol. Soc.*, *77*, 1275–1277.
- Madden, R. A. (2007), Large-scale, free Rossby waves in the atmosphere—An update, *Tellus, Ser. A*, *59*, 571–590, doi:10.1111/j.1600-0870.2007.00257.x.
- Madden, R. A., and P. R. Julian (1994), Observations of the 40–50-day tropical oscillation—A review, *Mon. Weather Rev.*, *122*, 814–837.
- Magaña, V., and M. Yanai (1995), Mixed Rossby-gravity waves triggered by lateral forcing, *J. Atmos. Sci.*, *52*(9), 1473–1486.
- Matsuno, T. (1966), Quasi-geostrophic motions in the equatorial area, *J. Meteorol. Soc. Jpn.*, *44*, 25–43.
- Morgenstern, O., et al. (2010), Review of present-generation stratospheric chemistry-climate models and associated external forcings, *J. Geophys. Res.*, *115*, D00M02, doi:10.1029/2009JD013728.
- Nishi, N., E. Nishimoto, H. Hayashi, M. Shiotani, H. Takashima, and T. Tsuda (2010), Quasi-stationary temperature structure in the upper troposphere over the tropical Indian Ocean inferred from radio occultation data, *J. Geophys. Res.*, *115*, D14112, doi:10.1029/2009JD012857.
- Nishimoto, E., and M. Shiotani (2012), Seasonal and interannual variability in the temperature structure around the tropical tropopause and its relationship with convective activities, *J. Geophys. Res.*, *117*, D02104, doi:10.1029/2011JD016936.

- Onogi, K., et al. (2007), The JRA-25 reanalysis, *J. Meteorol. Soc. Jpn.*, *85*(3), 369–432.
- Pan, C. J., U. Das, S. S. Yang, C. J. Wong, and H. C. Lai (2011), Investigation of Kelvin waves in the stratosphere using FORMOSAT-3/COSMIC temperature data, *J. Meteorol. Soc. Jpn.*, *89A*, 83–96.
- Press, W. H., S. A. Teukolsky, W. T. Vetterling, and B. P. Flannery (1992), *Numerical Recipes in FORTRAN: The Art of Scientific Computing*, 2nd ed., 963 pp., Cambridge Univ. Press, Cambridge, U. K.
- Randel, W. J., and F. Wu (2005), Kelvin wave variability near the equatorial tropopause observed in GPS radio occultation measurements, *J. Geophys. Res.*, *110*, D03102, doi:10.1029/2004JD005006.
- Ratnam, M. V., T. Tsuda, T. Kozu, and S. Mori (2006), Long-term behavior of the Kelvin waves revealed by CHAMP/GPS RO measurements and their effects on the tropopause structure, *Ann. Geophys.*, *24*, 1355–1366.
- Rienecker, M. M., et al. (2011), MERRA: NASA's Modern-Era Retrospective Analysis for Research and Applications, *J. Clim.*, *24*, 3624–3648, doi:10.1175/JCLI-D-11-00015.1.
- Saha, S., et al. (2010), The NCEP climate forecast system reanalysis, *Bull. Am. Meteorol. Soc.*, *91*(8), 1015–1057, doi:10.1175/2010BAMS3001.1.
- Scinocca, J. F., N. A. McFarlane, M. Lazare, J. Li, and D. Plummer (2008), The CCCma third generation AGCM and its extension into the middle atmosphere, *Atmos. Chem. Phys.*, *8*, 7055–7074.
- Selkirk, H. B., H. Vömel, J. M. Valverde Canossa, L. Pfister, J. A. Diaz, W. Fernández, J. Amador, W. Stolz, and G. Peng (2010), Detailed structure of the tropical upper troposphere and lower stratosphere as revealed by balloon sonde observations of water vapor, ozone, temperature, and winds during the NASA TCSP and TC4 campaigns, *J. Geophys. Res.*, *115*, D00J19, doi:10.1029/2009JD013209.
- Shibata, K., M. Deushi, T. T. Sekiyama, and H. Yoshimura (2005), Development of an MRI chemical transport model for the study of stratospheric chemistry, *Pap. Geophys. Meteorol.*, *55*, 75–119.
- Solomon, S., K. Rosenlof, R. Portmann, J. Daniel, S. Davis, T. Sanford, and G.-K. Plattner (2010), Contributions of stratospheric water vapor to decadal changes in the rate of global warming, *Science*, *327*, 1219–1223, doi:10.1126/science.1182488.
- Suzuki, J., and M. Shiotani (2008), Space-time variability of equatorial Kelvin waves and intraseasonal oscillations around the tropical tropopause, *J. Geophys. Res.*, *113*, D16110, doi:10.1029/2007JD009456.
- Suzuki, J., M. Fujiwara, A. Hamada, Y. Inai, J. Yamaguchi, R. Shirooka, F. Hasebe, and T. Takano (2010a), Cloud-top height variability associated with equatorial Kelvin waves in the tropical tropopause layer during the Mirai Indian Ocean cruise for the Study of MJO-convection Onset (MISMO) campaign, *Sci. Online Lett. Atmos.*, *6*, 97–100, doi:10.2151/sola.2010-025.
- Suzuki, J., M. Shiotani, and N. Nishi (2010b), Lifetime and longitudinal variability of equatorial Kelvin waves around the tropical tropopause region, *J. Geophys. Res.*, *115*, D03103, doi:10.1029/2009JD012261.
- Tsuda, T., Y. Murayama, H. Wiryosumarto, S. Harijono, and S. Kato (1994), Radiosonde observations of equatorial atmosphere dynamics over Indonesia: 1. Equatorial waves and diurnal tides, *J. Geophys. Res.*, *99*(D5), 10,491–10,505.
- Uppala, S. M., et al. (2005), The ERA-40 re-analysis, *Q. J. R. Meteorol. Soc.*, *131*(612), 2961–3012.
- Virts, K. S., and J. M. Wallace (2010), Annual, interannual, and intraseasonal variability of tropical tropopause transition layer cirrus, *J. Atmos. Sci.*, *67*, 3097–3112, doi:10.1175/2010JAS3413.1.
- Virts, K. S., J. M. Wallace, Q. Fu, and T. P. Ackerman (2010), Tropical tropopause transition layer cirrus as represented by CALIPSO lidar observations, *J. Atmos. Sci.*, *67*, 3113–3129, doi:10.1175/2010JAS3412.1.
- von Storch, H., and F. W. Zwiers (1999), *Statistical Analysis in Climate Research*, 484 pp., Cambridge Univ. Press, Cambridge, U. K.
- Wheeler, M., and G. N. Kiladis (1999), Convectively coupled equatorial waves: Analysis of clouds and temperature in the wavenumber-frequency domain, *J. Atmos. Sci.*, *56*, 374–399.
- World Meteorological Organization (2007), Scientific assessment of ozone depletion: 2006, *Global Ozone Res. Monit. Proj. Rep. 50*, 572 pp., Geneva, Switzerland.
- World Meteorological Organization (2011), Scientific assessment of ozone depletion: 2010, *Global Ozone Res. Monit. Proj. Rep. 52*, 516 pp., Geneva, Switzerland.